Hindawi
Advances in Civil Engineering
Volume 2024, Article ID 8818666, 23 pages
https://doi.org/10.1155/2024/8818666

Research Article

Experimental Study on the Seismic Performance of Insulated Single-Sided Composite Shear Walls under Different Shear Spans and Axial Compression Ratios

Qiang Sun,[1] **Shoufeng Zhang**,[1] **Ke Liu**,[1] **Xinyi Wu**,[1] **Guowei Zhang**,[2] **and Bei Cheng**[2]

[1]*China Architecture Design and Research Group, Beijing 100044, China*
[2]*Beijing University of Civil Engineering and Architecture, Beijing 100044, China*

Correspondence should be addressed to Qiang Sun; 2013119@cadg.cn

Received 16 May 2023; Revised 20 February 2024; Accepted 1 March 2024; Published 2 May 2024

Academic Editor: Giovanni Garcea

The new insulated single-sided composite shear wall (NISCSW) composition involves setting a precast wall panel on one side and an insulation panel on the other side, with a middle cavity for casting concrete. To investigate the seismic performance of NISCSW under different shear spans and axial compression ratios, eight specimens are made, including six composite and two cast-in-place walls. The shear span ratio is controlled at 1.2 and 1.9, and the axial compression ratio is controlled at 0.1, 0.3, and 0.4. The specimens are subjected to quasistatic tests to analyze failure modes, hysteresis characteristics, stiffness degradation, displacement ductility, and energy dissipation capacity and to compare the seismic performance of the composite and cast-in-place walls. Results show that for each composite specimen, under the same axial compression ratio, the large shear span ratio specimen has a lower ultimate bearing capacity and faster stiffness degradation but better ductility and postyield energy dissipation capacity. Under the same shear span ratio, the high axial compression ratio specimen had a higher ultimate bearing capacity, slightly worse ductility, and similar stiffness degradation and energy dissipation capacity compared to other specimens. Compared with the cast-in-place specimen with the same axial compression ratio, the composite specimen failure mode and hysteresis characteristics are similar, and the ductility and energy dissipation capacity are comparable to the cast-in-place shear wall specimen, indicating that NISCSW has similar seismic performance to the cast-in-place shear wall under conditions of a large shear span ratio and high axial compression ratio. Based on the test results, the program ABAQUS is used to simulate the specimens. Compared with the test results, the simulated specimen failure mode is consistent with the test results, and the hysteresis and skeleton curves are consistent with the test curve, indicating that the model is correct, reliable, and can be verified with test results.

1. Introduction

In recent years, there have been two commonly used methods for insulating precast exterior wall systems. One is to use precast concrete shear walls for the structure and add insulation after installation. This method is similar to the traditional method used in cast-in-place exterior wall systems, where the quality of the adhesion of insulation is greatly affected by human factors, making it difficult to ensure the durability of insulation. The surface of the precast components is coated with mold release agents during the production process, which affects the adhesion strength of the insulation to the face of the wall, resulting in low adhesion strength, and leaving the insulation prone to detachment from the wall face. Separating the fabrication of the walls and insulation can hardly meet the goal of improving the quality and efficiency of prefabricated building production.

The other method is to use a "sandwich" wall for the structure, where a precast shear wall panel is installed on one side, insulation is installed in the middle, and an outer concrete panel is placed on the other side. This method achieves the integration of the wall, insulation, and decorative elements and resolves the efficiency concern of constructing the exterior wall. However, the outer concrete panel is heavy, placing a high loading requirement on the connectors. The outer panel is prone to incurring damage during the lifting and transportation process, and the repair

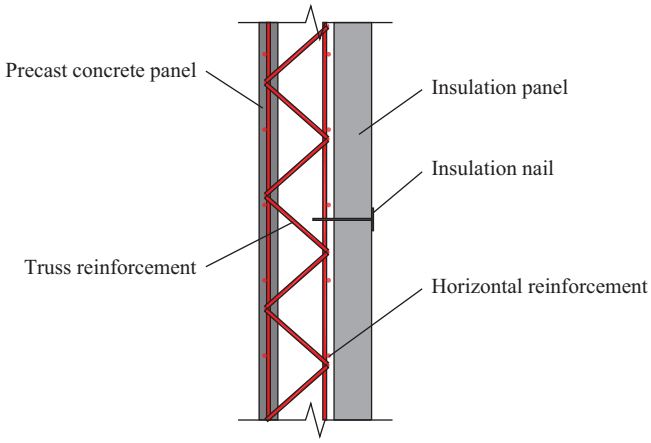

Figure 1: Diagram of NISCSW.

and protection of the panel are difficult. The temperature difference generated by the insulation layer causes structural thermal stress to occur between the inner and outer panels, placing the building in an unstable state year-round and significantly shortening the lifespan of the building structure.

Therefore, a new insulated single-sided composite shear wall (NISCSW) is proposed, as shown in Figure 1. This new type of composite shear wall is composed of an insulated composite wall panel component and cast-in-place concrete through reliable connectors. It has the advantages of being lightweight, high efficiency of installation, good durability, low cost of construction, and the ability to match the service life as the structure. The insulated composite wall panel component has a precast concrete wall panel (inner panel) on one side and an insulation panel on the other side, forming a cavity in the middle for cast-in-place concrete. The inner panel serves as part of the shear wall and also acts as an inner formwork during construction. The insulation panel serves as an external insulation layer and also acts as an outer formwork during construction. The insulation nail serves as a reliable connector between the insulation layer and the cast-in-place layer, preventing the insulation layer from falling off, but it does not serve as a structural load-bearing component.

Therefore, scholars from various countries have conducted extensive research on composite shear walls based on practical needs and have additionally focused on the study of the mechanical properties of composite shear walls under axial and lateral load conditions, mainly focusing on the out-of-plane bending behavior of the composite shear walls [1–4], compressive performance under axial and eccentric loads [5, 6], combined loading behavior and analysis [7, 8], thermal properties [9], vertical joints [10], and the performance of the connectors [11]. Because China is a country that experiences frequent earthquakes, Chinese scholars focus more on the seismic performance of the composite shear walls.

Composite shear walls can be classified into double-sided composite shear walls and single-sided composite shear walls (Figure 2) according to the composite situation, and the specific difference is whether the concrete outer panel participates in the load bearing. There are many studies on double-sided composite shear walls. Lian et al. [12–14] studied the seismic performance of double-sided composite shear walls, while Wang et al. [15, 16] studied the seismic performance of composite shear walls with confined boundary members [17] and with openings; the seismic performance of the horizontal joints [16, 18–20] and the vertical joints [21] of composite shear walls, T-shaped walls [22], walls with a vertical seam [23], and connectors [24] are also the focus of Chinese researchers. There are few studies focused on the seismic behavior of single-sided composite shear walls. Gu et al. [25], Ma et al. [26, 27], and Jiang et al. [28] have already conducted some research with this focus. However, the existing research conducted on single-sided composite shear walls still involves a concrete outer panel, and the investigations of the seismic performance of specimens without outer panels are still limited.

With the development of composite shear wall research and production technology, the maximum allowable application height of composite shear walls in China has increased from 60 to 80 m, and the concrete strength of low-level shear walls has been improved. The shear wall components near the bottom strengthening zone also show high axial compression ratio characteristics, and the axial compression ratio of some walls can reach 0.3–0.4. At the same time, due to the functional requirements of building energy savings and lighting, the proportion of large-sized windows used in design has increased, the length of the walls between windows has decreased, and the shear span ratio has increased. In multistory structures, the shear span ratio of walls between windows can reach 1.7–2.0. Composite shear walls are prone to being subjected to high axial compression and large shear span ratios in practical applications. At present time, the relevant research still has some deficiencies.

There has been some research conducted on composite shear wall performance when under a high axial compression ratio. Jiang et al. [28] studied the seismic performance of single-sided composite shear walls under axial compression ratios of 0.3 and 0.4 and concluded that the bearing capacity of the low axial compression ratio specimens is lower, but the ductility coefficient and energy dissipation coefficient are higher. Xue et al. [29] studied the in-plane and out-of-plane seismic performance of double-sided composite shear walls under an axial compression ratio of 0.5 and concluded that bending failure occurs on the double-sided composite shear walls when under a high axial compression ratio, with a higher ductility coefficient than the cast-in-place specimens, that the bearing capacity was approximately 11% different from the cast-in-place specimens, and the ductility coefficient of the specimens under a high axial compression ratio was slightly smaller. There is not much research available on the seismic performance of composite shear walls with a large shear span ratio, but Zhao et al. [30] studied the seismic performance of double-sided composite shear walls with a shear span ratio of 2 using prefabricated boundary elements. When comparing the results with other test data, the ductility coefficient of double-sided composite wall components under a large shear span ratio was larger.

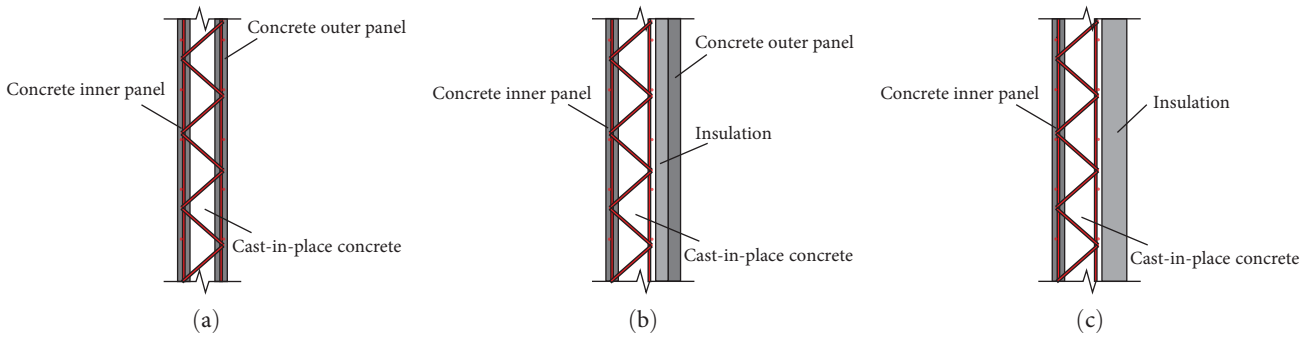

Figure 2: Classification of the composite shear walls: (a) double-sided composite shear wall, (b) single-sided composite shear wall, and (c) NISCSW, namely a single-sided composite shear wall without a concrete outer panel.

Table 1: Main specimen dimensions.

Specimen	Dimension of the top beam	Dimension of pedestal	Wall height	Wall width	Wall thickness
SW1-1	200 × 200 × 2,000	600 × 500 × 3,300	2,100	1,900	50/150/150
SW1-2	200 × 200 × 2,000	600 × 500 × 3,300	2,100	1,900	50/150/150
SW1-3	200 × 200 × 2,000	600 × 500 × 3,300	2,100	1,900	50/150/150
W1	200 × 200 × 2,000	600 × 500 × 3,300	2,100	1,900	-/200/-
SW2-1	200 × 200 × 1,800	600 × 500 × 3,100	2,900	1,700	50/150/150
SW2-2	200 × 200 × 1,800	600 × 500 × 3,100	2,900	1,700	50/150/150
SW2-3	200 × 200 × 1,800	600 × 500 × 3,100	2,900	1,700	50/150/150
W2	200 × 200 × 1,800	600 × 500 × 3,100	2,900	1,700	-/200/-

All dimensions for the top beams, pedestal, wall height, wall width, and wall thickness are in millimeters (mm). The dimensions for the top beams and pedestal are given as height × width × length. Wall height includes the 50 mm thick cast-in-place layer between the precast wall and the pedestal. The wall thickness is shown as a prefabricated layer/cast-in-place layer/insulation layer.

Therefore, to explore the seismic performance of NISCSW under different axial compression ratios and shear span ratios, specifically under conditions of high axial compression and large shear span ratios, this paper identifies the following methodology: design of specimens with shear span ratios of 1.2 and 1.9, conduct low-cycle horizontal reciprocating tests under axial compression ratios of 0.1, 0.3, and 0.4 and study the failure modes and crack distribution, analyze their failure mechanisms, bearing capacity, stiffness degradation, and energy dissipation capacity, compare and analyze them with cast-in-place shear wall specimens under the same test conditions, conduct finite element analysis on specimens with a shear span ratio of 1.9, and compare it with the test results to provide references for the practical application of this type of wall.

2. Test Program

2.1. Design of the Specimens. In this experiment, three groups of eight specimens were designed and fabricated: SW1-1, SW1-2, SW1-3, SW2-1, SW2-2, SW2-3, W1, and W2. Among them, SW1-1∼3 and SW2-1∼3 are NISCSW specimens, and W1 and W2 are cast-in-place concrete shear wall (CCSW) specimens. The shear span ratio of SW1-1∼3 and W1 is 1.2 and that of SW2-1∼3 and W2 is 1.9. The axial compression ratio of SW1-1 and SW2-1 is 0.1, that of SW1-2 and SW2-2 is 0.3, and that of SW1-3, SW2-3, W1, and W2 is 0.4. The specimen is composed of the top beam, the shear wall (including the wall and boundary elements), and the pedestal. The dimensions of the top beam and pedestal can be found in Table 1. Among them, SW1-1∼3 have a wall height of 2,100 mm, SW2-1∼3 have a wall height of 2,900 mm, and all heights include a 50 mm thick cast-in-place layer between the shear wall and the pedestal. W1 has a wall height of 2,100 mm, and W2 has a wall height of 2,900 mm. SW1-1∼3 and W1 have a width of 1,900 mm, and SW2-1∼3 and W2 have a width of 1,700 mm. The total thickness of the composite specimens is 350 mm, including a 50 mm precast layer, a 150 mm cast-in-place layer, and a 150 mm insulation layer. The insulation layer is formed in the manner of a double-layer insulation board, with graphite extruded board as the inner insulation panel and reinforced vertical rock wool composite board as the outer insulation panel. The thickness of the cast-in-place specimens is 200 mm. The horizontal and vertical distribution of the reinforcing bars in each specimen is D8@200 (the diameter of the steel bars is 8 mm, and the spacing between the steel bars is 200 mm), and the reinforcement ratio of the wall is 0.25%. The main information of the specimens is shown in Table 2, and the geometric dimensions and reinforcement of the specimens are shown in Figure 3.

2.2. Test Setup and Loading Scheme. The test loading device consists of a vertical loading device and a horizontal loading device (Figure 4(a)). The top of the insulated composite wall panel is slightly lower than the bottom of the wall beam, which does not affect the application of the load. The vertical load is applied synchronously to the top beam by two

Table 2: Main specimen information.

Specimen	Specimen type	Position	Shear span ratio	Axial compression ratio	Reinforcement ratio of longitudinal reinforcement of boundary elements (%)	Volume stirrup ratio of boundary elements (%)
SW1-1	Composite wall	Linear wall	1.2	0.1	1.16	1.45
SW1-2	Composite wall	Linear wall	1.2	0.3	1.16	1.45
SW1-3	Composite wall	Linear wall	1.2	0.4	1.5	1.45
W1	Cast-in-place wall	Linear wall	1.2	0.4	1.5	1.45
SW2-1	Composite wall	Wall between windows	1.9	0.1	1.16	1.45
SW2-2	Composite wall	Wall between windows	1.9	0.3	1.16	1.45
SW2-3	Composite wall	Wall between windows	1.9	0.4	1.5	1.45
W2	Cast-in-place wall	Wall between windows	1.9	0.4	1.5	1.45

hydraulic jacks, and a track is installed between the jack base and the distribution frame to ensure that the line of action of the vertical load is always perpendicular to the ground. The horizontal load is applied by a horizontal actuator. As shown in Figure 4(b), the vertical actuator loading plate is at one-third of the loading beam, and the wall beam is located at the exact center of the horizontal actuator loading plate. During the test, the actuators were well-fixed and there was no slippage or misalignment. To prevent safety accidents caused by the collapse of components, the steel structure bracings are installed on both sides of the wall.

First, a vertical load is applied to the top of the specimen and kept at a constant load after reaching the predetermined test axial compression ratio. The horizontal loading mode is a low-cycle reciprocating slow loading, and the loading method of the load–displacement hybrid control is adopted according to the Chinese Code of Specification for Seismic Test of Buildings (JGJ/T101-2015) [31]. The first stage is a load-controlled loading stage, with a 100 kN increment considered as one level of loading, and there is one loading cycle per level. After 500 kN has been applied, the load increment for each level is now applied in 50 kN increments and cycles once per level until the specimen yields. The second stage is displacement-controlled loading, with each level increment being 0.5 times the yield displacement of the specimen and with three cycles occurring per level. When the load drops to 85% of the peak load, the specimen is considered to have reached a state of failure, and the loading is stopped. During loading, push–pull loading is performed according to the loading system shown in Figure 5.

2.3. Test Measurement Scheme. To measure the changes in the horizontal displacement of the specimen, displacement meters are set on the vertical centerline of the height axis for each specimen. The displacement at the top beam loading point of the shear wall is measured by two linear displacement meters installed on the top beam. Two linear displacement meters are arranged on both sides at a height of half of the pedestal to determine the pedestal displacement and to avoid the influence of the sliding of the pedestal on the data. The positions of the test displacement meters are shown in Figure 6.

To study the failure mode and strain law of the specimens, concrete strain gauges and reinforcement strain gauges are used for measurement purposes. The concrete strain gauges are arranged mainly in the lower one third of the height of the shear wall where cracks are earlier to appear. The reinforcement strain gauges are arranged primarily at different heights of the steel mesh inside the shear wall and the reinforcement in the pedestal, and the measuring points are located at heights of 100, 450, and 850 mm from the top surface of the pedestal and one third of the lower part of the shear wall, where the steel bars yield earlier. The positions of the specimen strain gauges are shown in Figure 7.

2.4. Test Phenomenon and Failure Mode. The main failure processes and modes of each specimen are similar, which are controlled by the crushing of the concrete in the compression zone, longitudinal steel bars bending deformation at the edge of the compression zone, and the fracture of the longitudinal steel bars and stirrups in the tension zone. Therefore, SW1-3 and SW2-3 are taken as examples for discussion. The crack patterns of each specimen are shown in Figure 8.

2.5. SW1-3 (with an Axial Compression Ratio of 0.4 and a Shear Span Ratio of 1.2). At first, the specimen was basically in an elastic working state without any apparent signs of cracking, and there was no significant increase in the strain data of the concrete and steel bars in each part. When the applied horizontal load reached 700 kN, the first crack appeared at the lower part of the boundary element on one side of the specimen. When loaded to 950 kN, the steel bars in the middle and lower parts of the boundary elements on both sides of the specimen generally yielded. At this time, obvious cracks appeared along the diagonal direction on both sides of the wall and intersected in the middle of the wall to form an X shape, with the angle between the cracks and the horizontal direction slightly larger than 45°. Then, the cracks mostly continued to propagate. When the horizontal displacement was loaded to 29 mm, the specimen reached a peak load of 1,341 kN. At this time, the concrete crushing at the lower part of the boundary elements on both sides of the specimen was more serious, and the concrete cracks at the interface of the precast layer and the boundary elements increased. When the horizontal displacement was

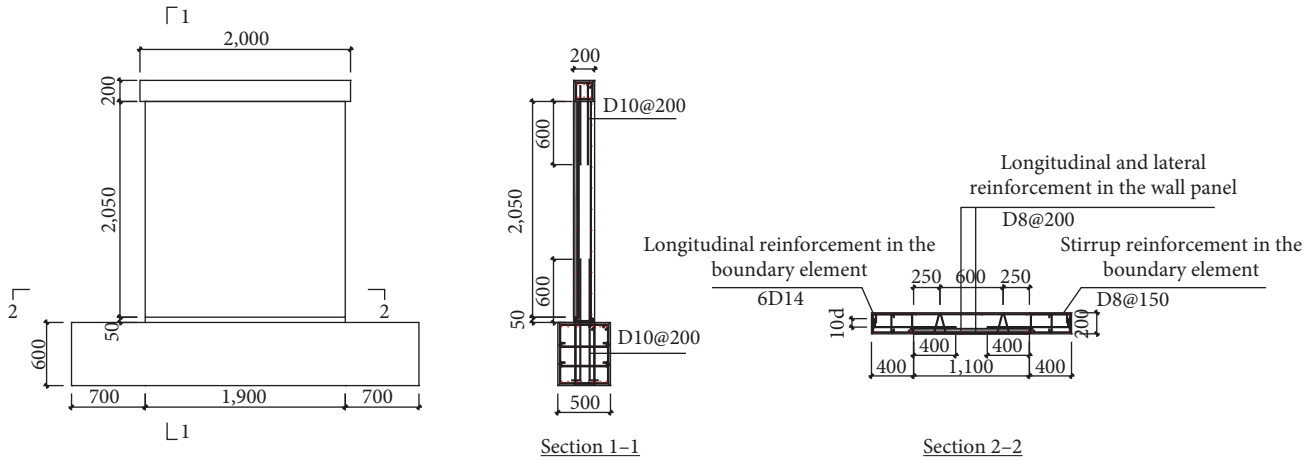

(a)

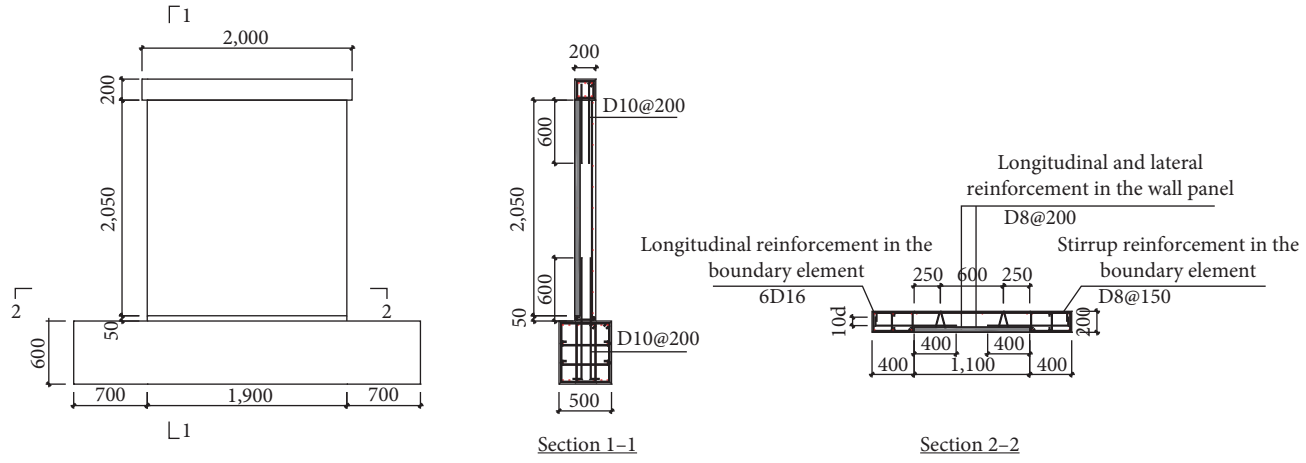

(b)

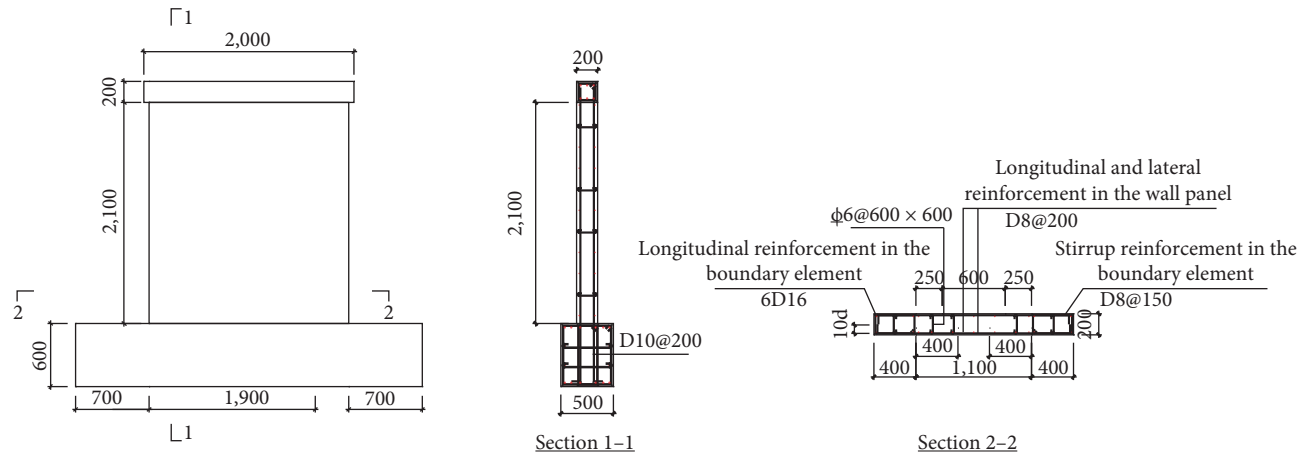

(c)

Figure 3: Continued.

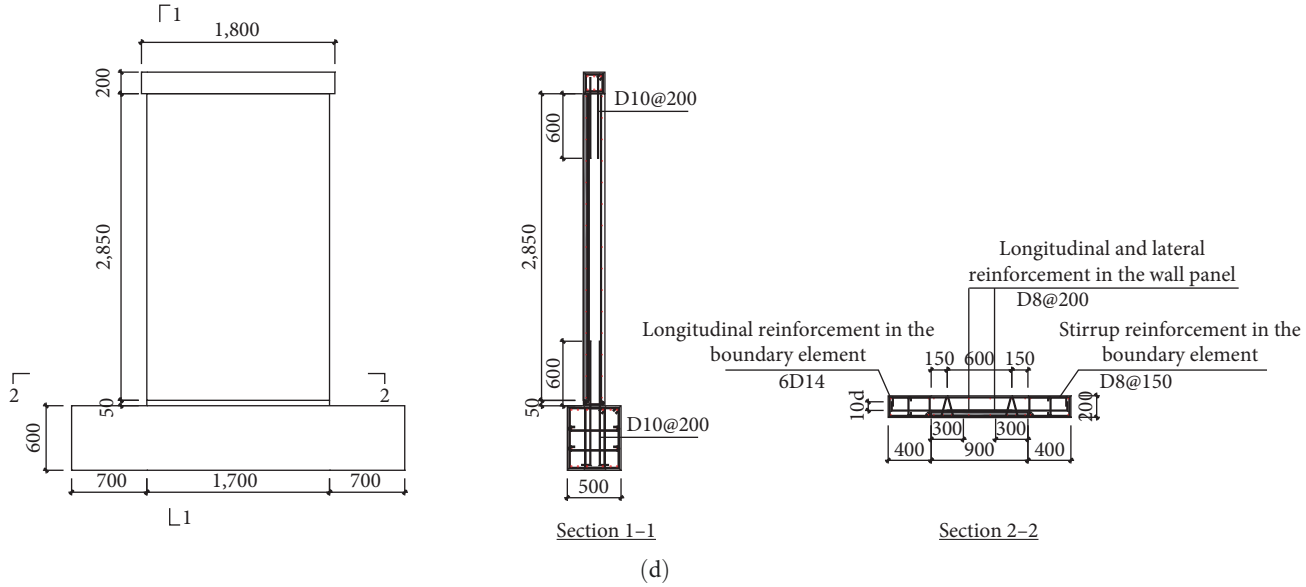

(d)

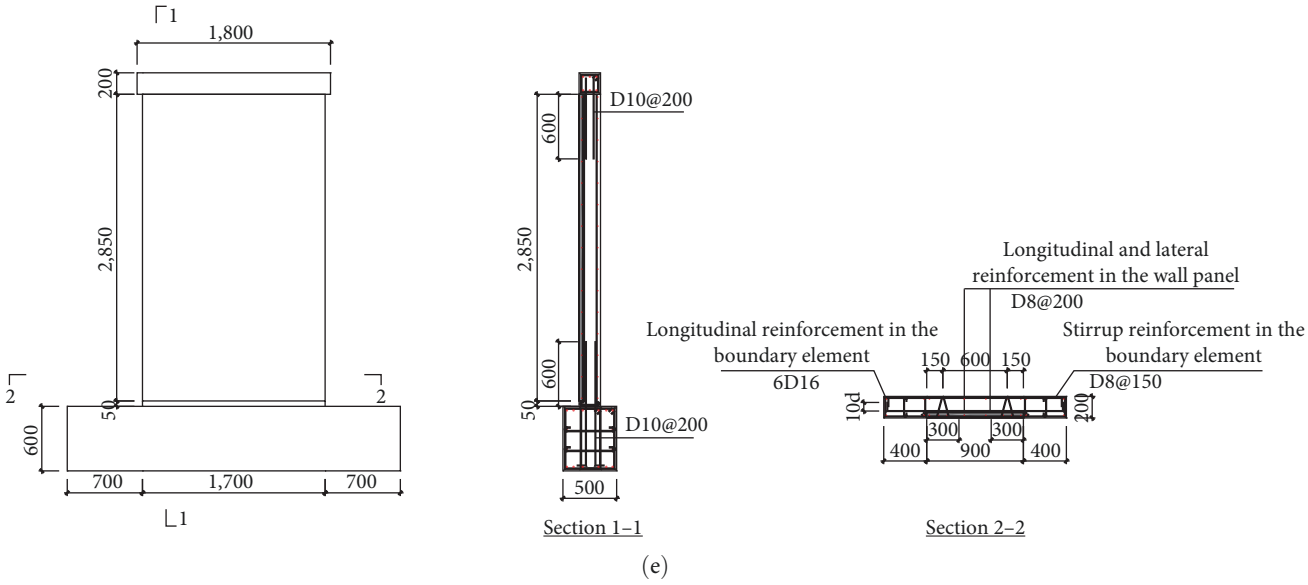

(e)

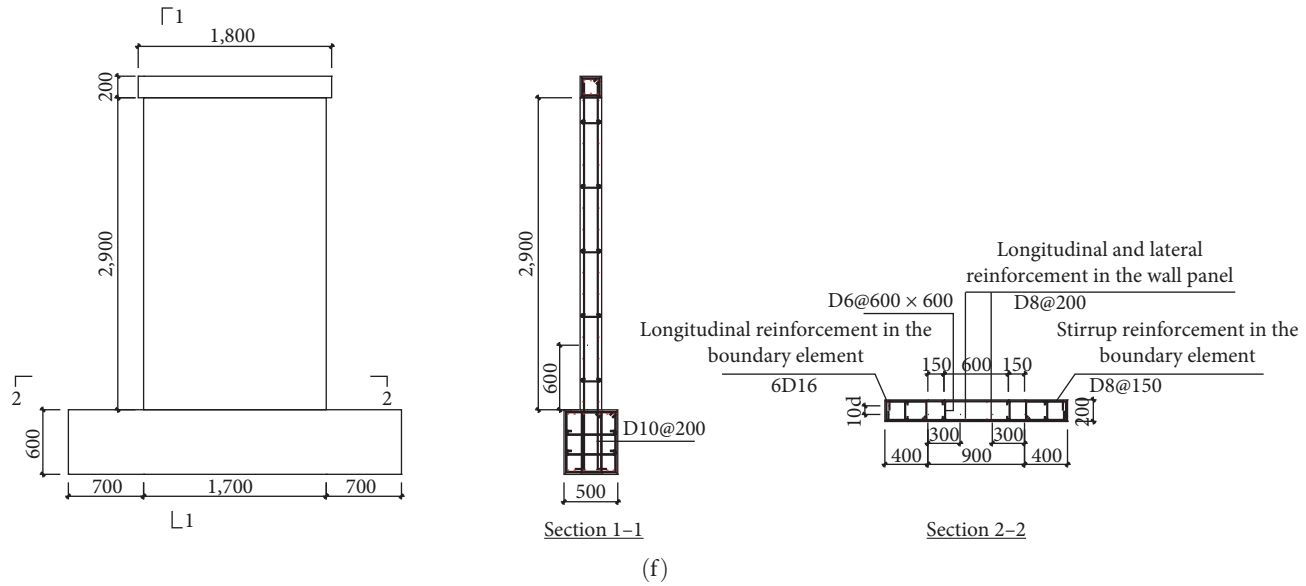

(f)

Figure 3: Dimensions and steel reinforcement layout of specimens: (a) SW1-1∼2, (b) SW1-3, (c) W1, (d) SW2-1∼2, (e) SW2-3, and (f) W2.

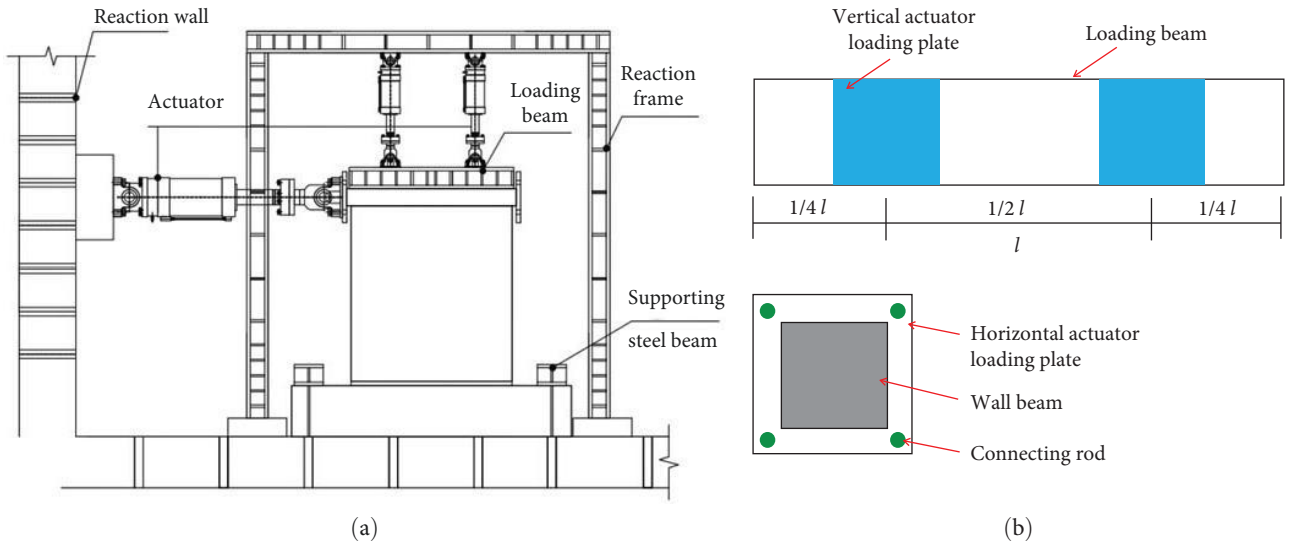

Figure 4: (a) Test setup and (b) loading position.

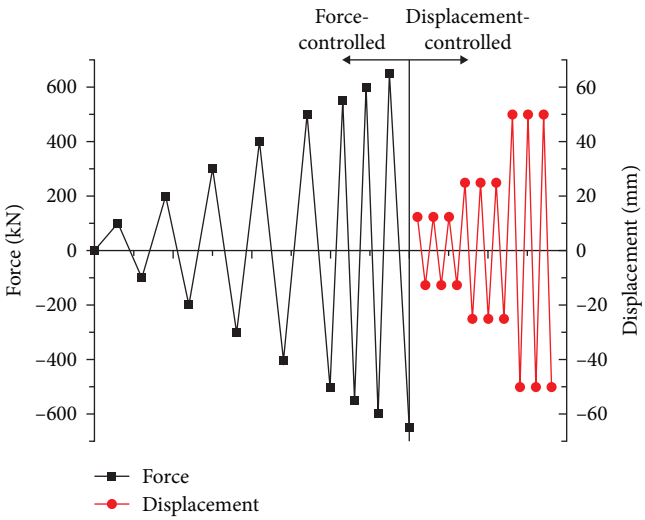

Figure 5: Loading system.

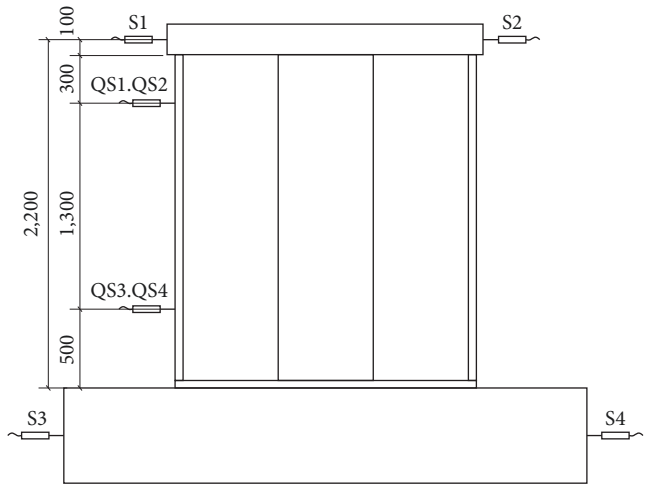

Figure 6: Positions of the test displacement meters.

loaded to 30 mm for the second cycle, at the lower part of the shear wall, the longitudinal reinforcement yielded, the stirrup and the interface between the insulation layer and the cast-in-place layer were detached, the insulation nails were embedded in the vertical wire rock wool layer, the cast-in-place concrete layer between the wall and the pedestal was compressed and then destroyed, and there was slight slippage between the lower part of the precast layer and the boundary elements. Finally, when the displacement was loaded to 30 mm in tension, the concrete at the bottom of the shear wall was compressed and broke, the steel bars yielded, the horizontal load decreased to 85% of the peak load, and the test was ended. During the entire test process, although the insulation layer was partially detached from the cast-in-place layer, it did not fall off, and the connectors effectively connected the insulation panel and the structural layer. Figure 9(a) shows the details of the failure mode of SW13.

2.6. SW2-3 (with an Axial Compression Ratio of 0.4 and a Shear Span Ratio of 1.9). At first, the behavior of the specimen was basically the same as that of SW1-3. When the horizontal load reached 350 kN, two horizontal flexural cracks appeared at a height of 320 mm above the shear wall edge. When loaded to 650 kN, multiple horizontal cracks appeared in the height direction of the shear wall, and the cracks were extended to 1.2 m along the height of the wall. The horizontal flexural cracks extended to the precast layer and developed into diagonal flexural-shear cracks, and the longitudinal reinforcement of the boundary elements yielded. Subsequently, cracks continued to develop and were concentrated at the root of the wall. The flexural-shear cracks on both sides intersected in the middle of the shear wall, all the longitudinal reinforcement of the boundary elements yielded, and the concrete on the tensile side cracked. When the horizontal displacement was loaded to 29 mm, the

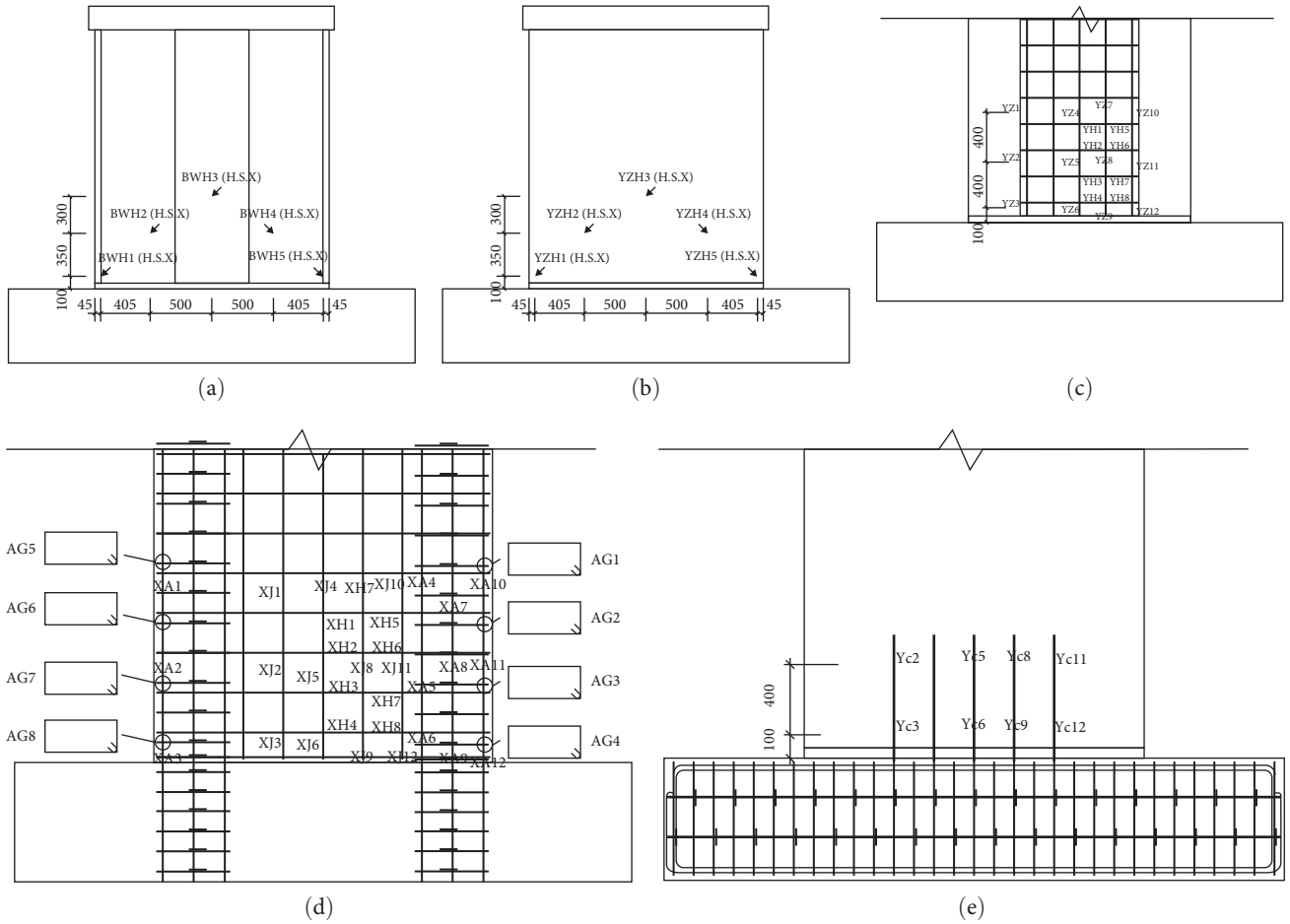

FIGURE 7: Strain gauge positions: (a) strain gauge positions of insulation, (b) strain gauge positions of the concrete inner panel, (c) strain gauge positions of reinforcement in the precast panel, (d) strain gauge positions of reinforcement in the cast-in-place concrete, and (e) strain gauge positions of insert reinforcement.

specimen reached its peak loading condition of 833 kN, and a small area of concrete relaxation occurred at the root of the wall on the compression side. The long crack at the interface between the shear wall and the pedestal deepened. When the horizontal displacement reached 36 mm, all the longitudinal and stirrup bars below the 200 mm height of the boundary elements were exposed, and the outermost longitudinal bars of the boundary elements were compressed and then yielded. The insulation layer was separated from the structural layer at a position of 300 mm from the bottom of the insulation layer, and the insulation layer itself was well combined without delamination present. When the horizontal displacement was loaded to 36 mm for the third cycle, the longitudinal and stirrup bars at the edge of the tensile side of the wall broke, the horizontal load of the specimen decreased to 85% of the peak load, and the test ended. Figure 9(b) shows the details of the failure mode of SW2-3.

2.7. Failure Mode of the Specimen. From the experimental results, it can be seen that cracks generally appear from the boundary element first. Then, they appear at the interface of the wall and the pedestal and extend to the surface of the wall, gradually developing from horizontal cracks into diagonal ones, ultimately forming an X-shape. Under the same loading conditions, the failure modes of the composite specimens and cast-in-place specimens are basically the same. For the composite specimens, there are no longitudinal gaps, slips, or dislocations occurring between the precast layer and the cast-in-place layer, indicating that the steel bars effectively tie the precast layer and the cast-in-place layer together, ensuring the two layers have a coordinated working relationship.

As the axial compression ratio increases, the appearance of the first crack of each specimen is delayed, and the propagation of cracks is inhibited, resulting in a decrease in the height of the crack intersections. Besides, the bottom of the insulation layer gradually separates from the structural layer. When the axial compression ratio is 0.1, there are no cracks on the surface of the insulation layer, and there is no slip or dislocation occurring between the insulation layer and the structural layer. However, under the high axial compression ratios of 0.3 and 0.4, the bottom 400 mm area of the insulation layer and the structural layer collapses, and the insulation nails are embedded. This is because the concrete at the edge of the compression zone is seriously crushed under conditions of high axial compression ratios. At this time, the insulation nails fulfill a connecting role between the

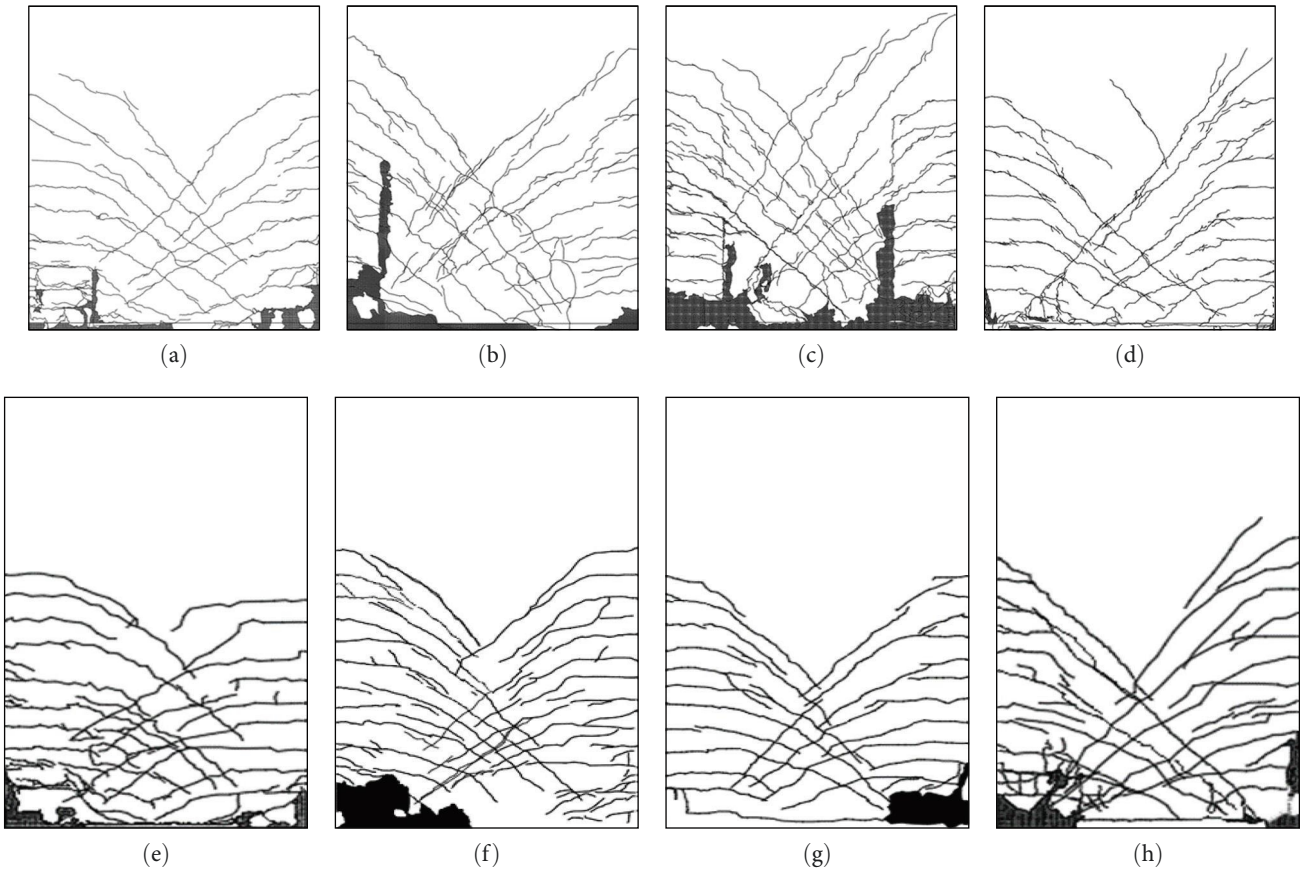

Figure 8: Crack patterns of each specimen (a) SW1-1, (b) SW1-2, (c) SW1-3, (d) W1, (e) SW2-1, (f) SW2-2, (g) SW2-3, and (h) W2.

insulation layer and the cast-in-place layer, improving the overall stability of the specimens.

As the shear span ratio increases, the failure mode of the specimens gradually transitions from a flexural-shear failure to a bending failure, and the height of the intersections of the cracking decreases.

3. Test Results and Analysis

3.1. Hysteresis Curve. The hysteresis curves of each specimen have similar characteristics, as shown in Figure 10. At the beginning of the test, the hysteresis loops of the specimen are relatively symmetrical in the positive and negative loading directions. The hysteresis curves are straight lines, the hysteresis loops are narrow and long, and the enclosed area is small. The reduction in the slope of the curves under the same loading direction is not significant, and the hysteresis loops coincide. The specimen is in an elastic working state, and the stiffness is essentially unchanged. The slope of the hysteresis curve increases with an increasing axial compression ratio. As the cracks develop, the hysteresis curve inclines to the displacement axis, the hysteresis loop area significantly increases, and the shape is full. The deformation of the wall increases, and the hysteresis curves cannot overlap. As the displacement control stage is reached, with the gradual increase in the displacement, the peak load of each hysteresis loop shows an increasing and then a decreasing trend. The shape of the hysteresis curve changes from a spindle to that of a reverse S-shape, and the hysteresis curve exhibits a certain amount of pinching.

Under the same shear span ratio and with the increase in the axial compression ratio, the stiffness of the steel bars increases in the loading stage before reaching its yield state, and the hysteresis loop pinching phenomenon during the displacement loading stage decreases. The fullness level changes slightly, and the energy dissipation capacity of each specimen is the same. At the same time, with the increase in the axial compression ratio, the initial stiffness of the specimen increases successively, and the peak load increases significantly.

Under the same axial compression ratio, compared with the specimens with different shear span ratios, the specimens with a large shear span ratio have a lower ultimate bearing capacity and a smaller hysteretic loop area. Compared with the cast-in-place specimens with the same axial compression ratio, the fullness of the hysteresis loop of the composite specimen is the same as that of the cast-in-place specimen, and the energy dissipation capacity is the same.

3.2. Skeleton Curve and Stiffness Degradation Curve. Connecting the peak points of each hysteresis curve, the skeleton curves of each specimen are obtained, as shown in Figure 11. In the early loading stage, the skeleton curves of each specimen are straight lines and essentially coincide, and the

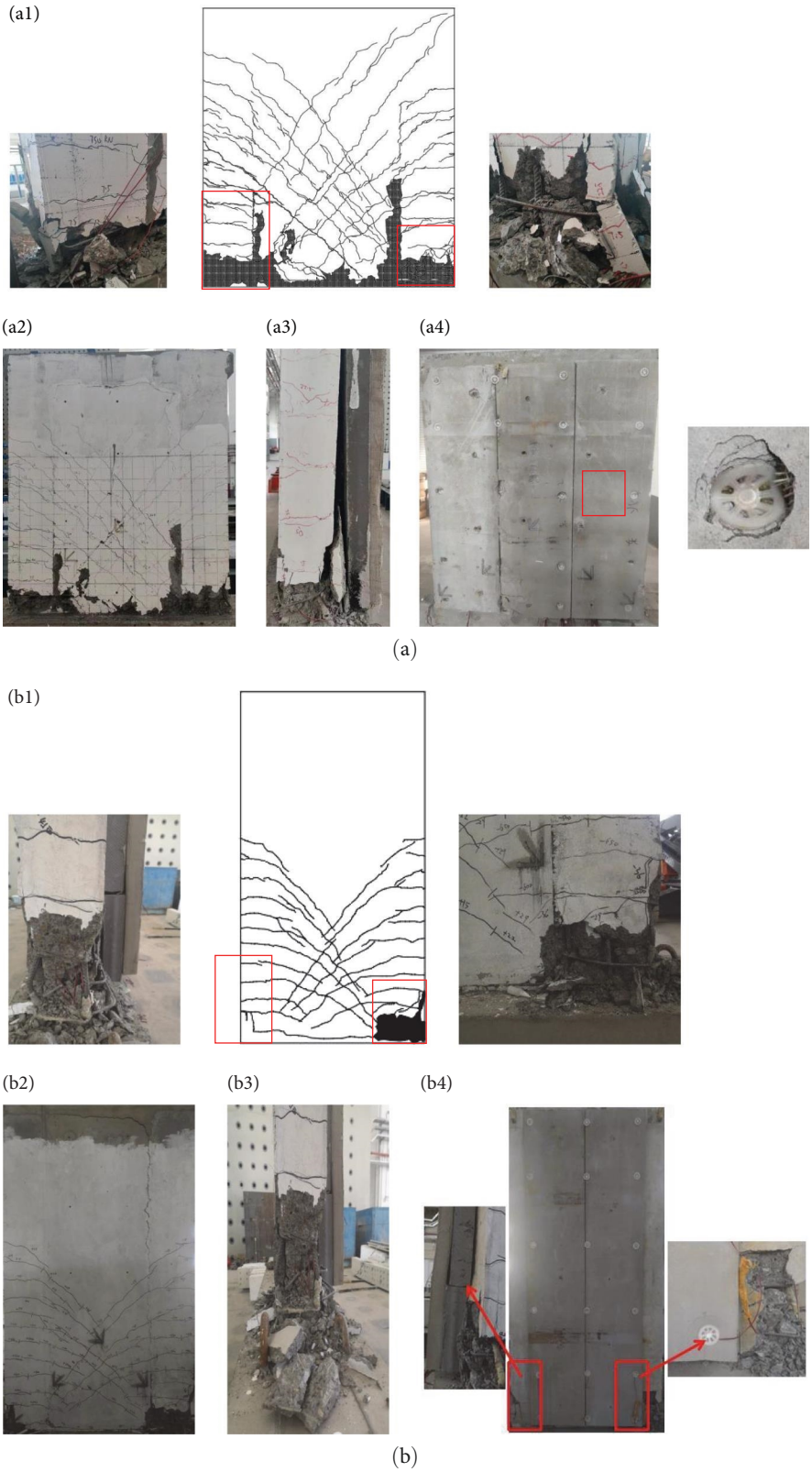

Figure 9: Failure mode of each specimen. (a) SW1-3. (b) SW2-3. (a1 and b1) Crack trends at the failure stage. (a2 and b2) Failure mode of the wall. (a3 and b3) Failure mode of the side of the specimen. (a4 and b4) Failure mode of the insulation layer.

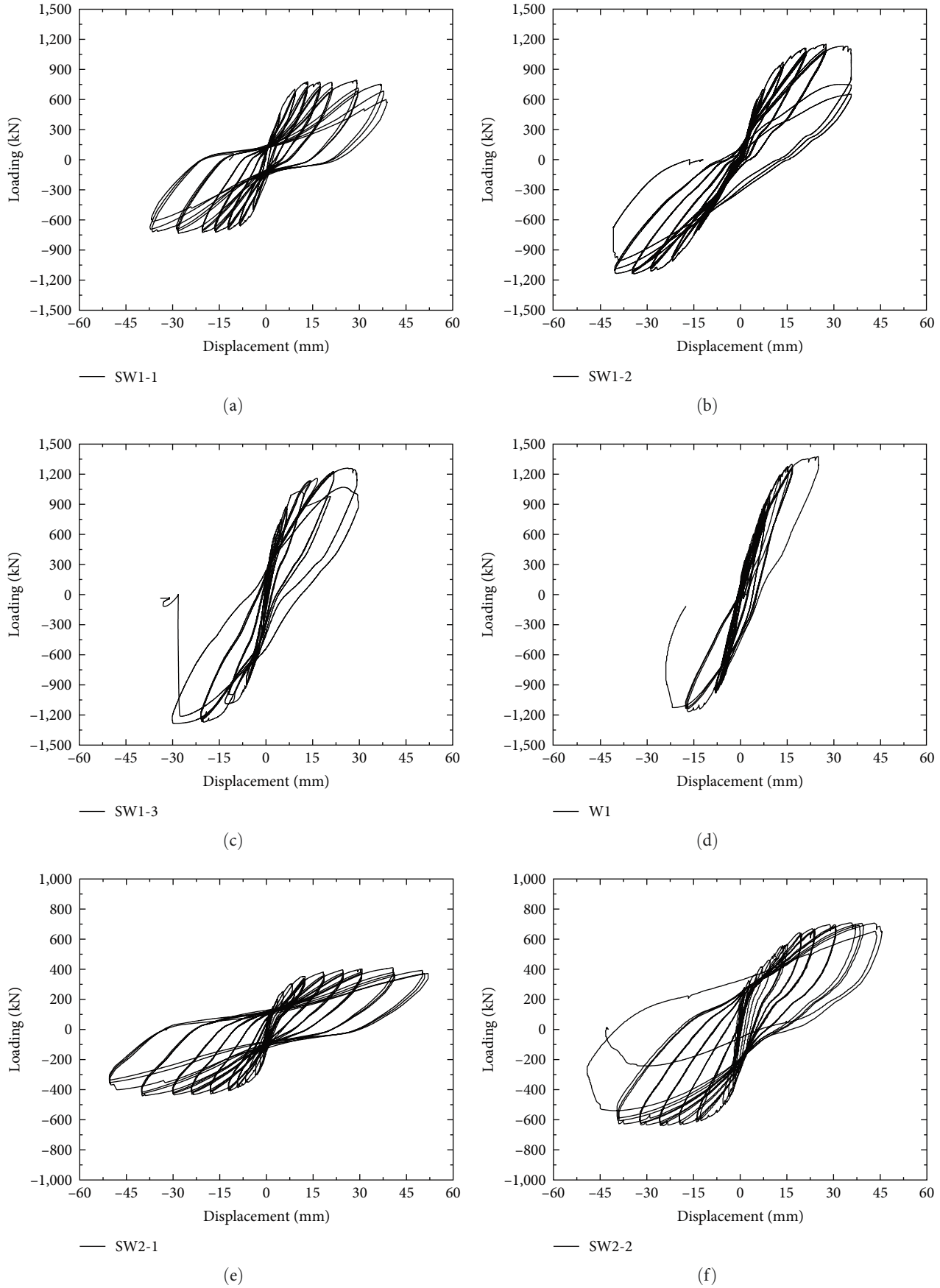

Figure 10: Continued.

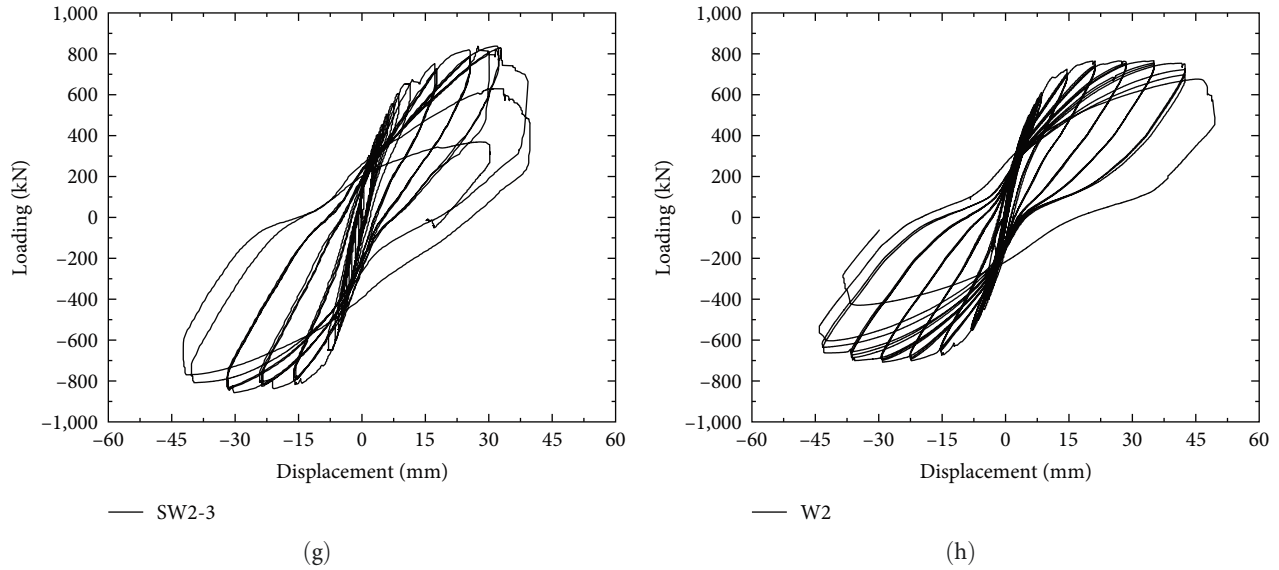

Figure 10: Hysteresis curves of the specimens: (a) SW1-1, (b) SW1-2, (c) SW1-3, (d) W1, (e) SW2-1, (f) SW2-2, (g) SW2-3, and (h) W2.

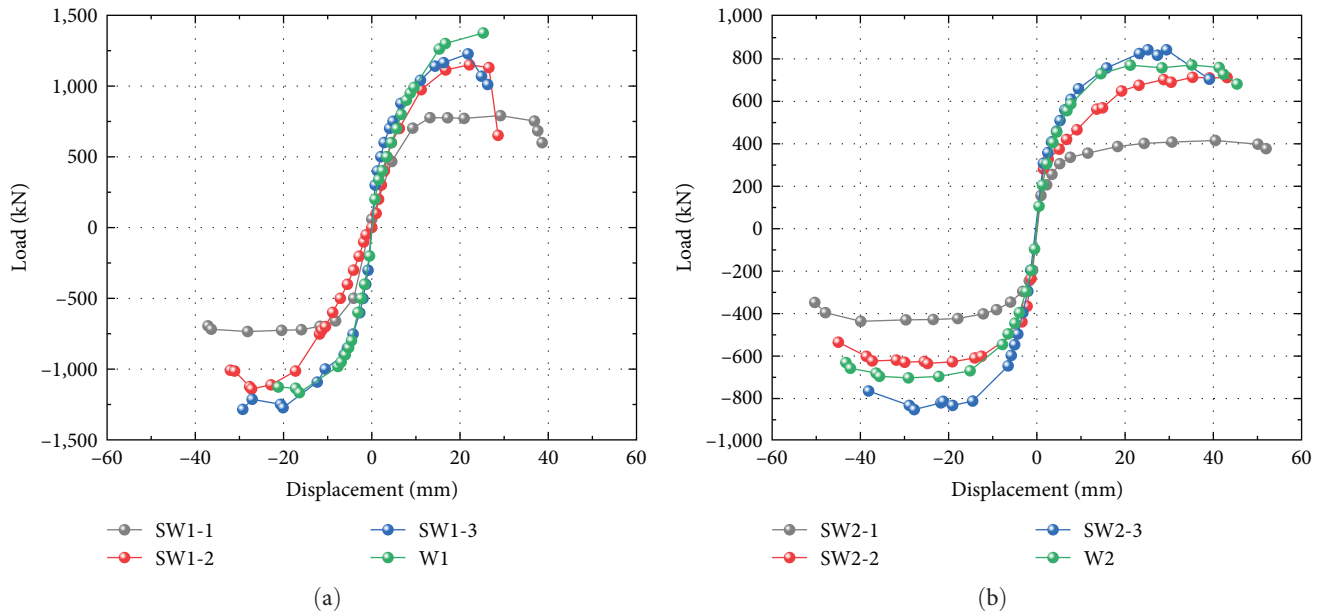

Figure 11: Skeleton curves of the specimens: (a) SW1-1∼3 and W1 series. (b) SW2-1∼3 and W2 series.

specimen is in the elastic stage. In the early stage, the stiffness and lateral displacement of each specimen changed a small amount. As further cracks develop, the skeleton curve begins to approach the displacement axis, and the slope of the curve decreases. After reaching the peak point, the slope of the skeleton curve becomes negative, and the bearing capacity and overall stiffness of the specimens decrease.

Under the same shear span ratio, as the axial compression ratio increases, the ultimate bearing capacity of the specimen gradually increases, the skeleton curve after the peak point decreases rapidly, the smooth section becomes shorter, and the ductility of the specimen decreases. Compared with SW1-1 and SW2-1 under the condition of a low axial compression ratio, the peak loads of SW1-2∼3 and SW2-2∼3 under the high axial compression ratio condition increases by 45%–97%, but the deformation capacity decreases and the slope of the descending section is larger. This is because the increase in the axial load inhibits the development of cracks and improves the bearing capacity but also increases the crushing area of the concrete in the compression zone, leading to a decrease in the ductility of the specimen.

Under the same axial compression ratio, as the shear span ratio increases, the peak load and ultimate bearing capacity of the specimen decrease, the smooth section of the curve becomes longer, and the ductility is better. The peak load of the large shear span ratio specimen is

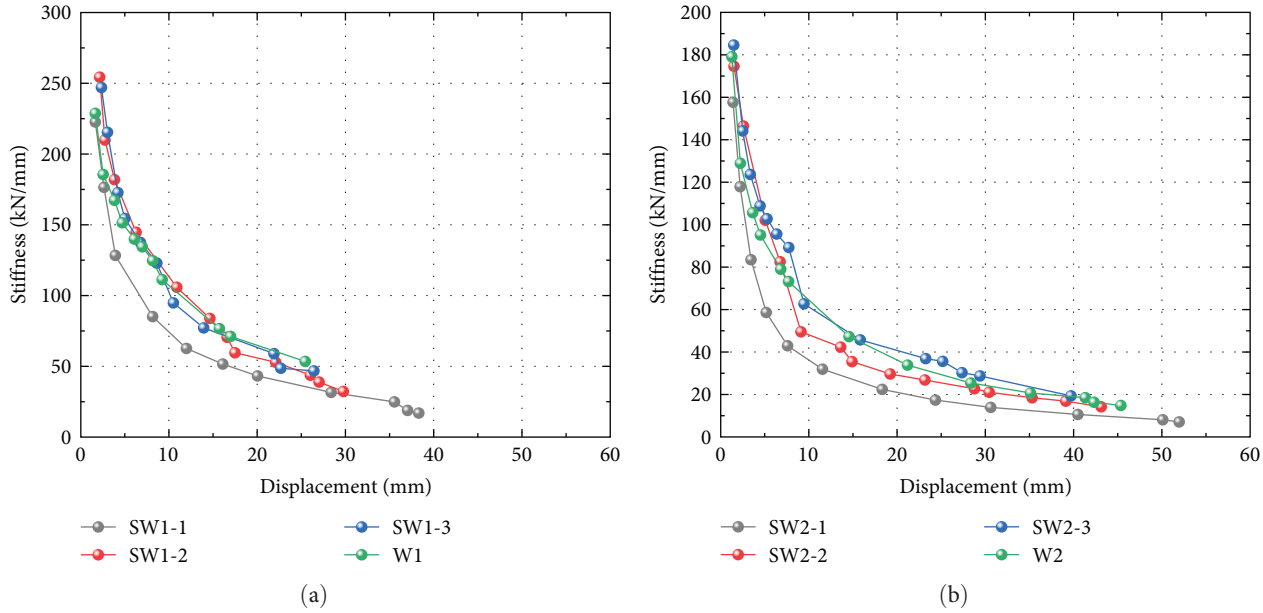

Figure 12: Stiffness degradation curve of the specimens: (a) SW1-1~3 and W1 series. (b) SW2-1~3 and W2 series.

Table 3: Experimental results at the main stages of testing development.

Specimen	Cracking displacement (mm)	Cracking load (kN)	Yield displacement (mm)	Yield load (kN)	Peak displacement (mm)	Peak load (kN)	Ultimate displacement (mm)	Displacement ductility coefficient, μ	Ultimate displacement angle θ p
SW1-1	3.98	290	9.28	702	29.16	788	37.68	4.06	1/57
SW1-2	2.84	337	9.72	965	25.68	1,143	29.45	3.29	1/62
SW1-3	3.06	428	10.21	1,121	29.26	1,350	29.84	2.92	1/55
W1	4.43	510	11.77	1,054	25.25	1,357	25.65	2.18	1/88
SW2-1	4.53	200	12.89	410	40.48	375	50.15	3.89	1/58
SW2-2	4.16	256	14.76	585	39.65	649	45.99	3.1	1/66
SW2-3	3.95	284	15.56	757	29.97	833	39.46	2.6	1/75
W2	3.64	305	14.32	790	41.32	680	45.35	3.17	1/64

approximately only 55% of the value as that of the small shear span ratio specimen, but the extreme displacement increases by more than 30%.

Compared with the cast-in-place specimens, the skeleton curve of the composite specimens in the early stage is the same as that of cast-in-place specimens. The bearing capacity is not much different from that of the cast-in-place members, and the seismic performance is good. Comparing the skeleton curves of the composite specimens and the cast-in-place specimens, it can be seen that there is little difference in the peak load between them in the range of the positive skeleton curves, but the peak load of the composite specimens is higher in the negative skeleton curves. This may be because the composite specimens are not completely symmetrical, and the shear walls usually crack at small displacement angles, resulting in certain differences between the positive and negative skeleton curves.

Figure 12 shows the specimen stiffness degradation curve. As shown in Figure 12, the stiffness degradation trend of each specimen is the same. Before yielding, the stiffness degradation curves of each specimen coincide, and the stiffness degradation rate of the specimens is rapid due to crack formation and development. After yielding, the stiffness degradation rate of the specimen slows down. The initial stiffness of the composite specimen is a little higher than that of a cast-in-place specimen, but the initial stiffness degradation rate of the composite specimen is much higher, which is due to the insufficient compactness of the 50 mm thick cast-in-place concrete layer between the shear wall and the pedestal during the composite specimen fabrication process, but it has little influence on the stiffness of the specimens. Under the same axial compression ratio, the initial stiffness of the large shear span specimen is smaller. Under the same shear span ratio, the ductility of the low axial compression ratio specimens is better.

3.3. Displacement Ductility and Energy Dissipation Capacity. The load and displacement characteristic values, the displacement ductility coefficients, and the ultimate displacement angles of each specimen are shown in Table 3.

Analysis of the information displayed in Table 3 shows that the displacement ductility coefficients of the small shear

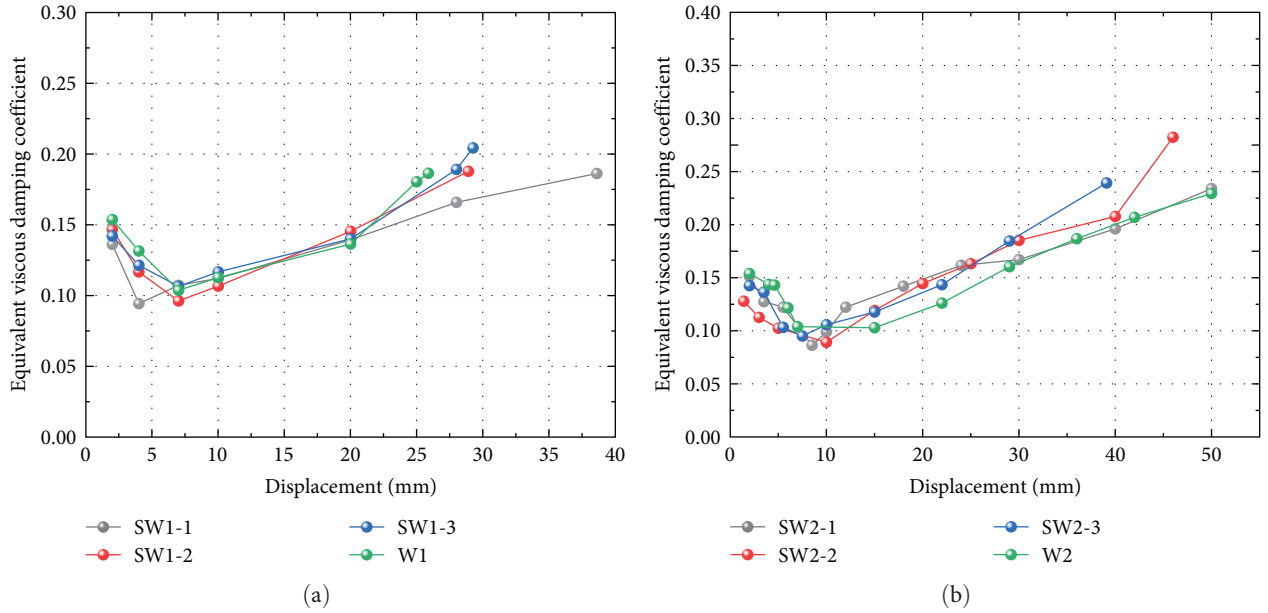

Figure 13: Equivalent viscous damping coefficient curves of the specimens: (a) SW1-1~3 and W1 series. (b) SW2-1~3 and W2 series.

span ratio composite specimens are higher than those of the cast-in-place specimens. The displacement ductility coefficients of the large shear span ratio composite specimens are the same as those of the cast-in-place members, but under the same axial compression ratio, the displacement ductility coefficients of the composite specimens are lower than those of the cast-in-place specimens with an approximately 20% difference. This indicates that the ductility of the composite specimens is comparable to that of the cast-in-place specimens, and the smaller displacement ductility coefficients of the W1 specimen may be related to the poor quality of the specimen due to inadequate vibration during fabrication. At the same time, with the axial compression ratio increase, the displacement ductility coefficients of the composite specimens decreased by more than 40%, with a larger decrease for the large shear span ratio specimens, indicating that a high axial compression ratio and a large shear span ratio have a greater impact on the ductility of the specimens. However, the maximum ultimate displacement angle of all specimens is 1/55, which is much larger than the limit value of 1/120 for the displacement angle under rare earthquakes specified in the Chinese Code of Seismic Design of Buildings (GB50011-2010) [32], indicating that each specimen meets the shear wall deformation capacity requirements in current Chinese codes.

The equivalent viscous damping coefficients of each specimen are shown in Figure 13, and as shown, the trends of the equivalent viscous damping coefficient of each specimen are the same, showing a trend of decreasing initially and then increasing with a corresponding increasing displacement. In the elastic stage, the equivalent viscous damping coefficient decreases because the specimen is initially in the elastic stage, with less energy dissipation and an increase in the elastic energy. Compared with the cast-in-place specimens, the equivalent viscous damping coefficient of the composite specimens is slightly smaller. As the specimen enters the elastic–plastic stage, the hysteretic loop becomes full, the energy dissipation increases rapidly, and the equivalent viscous damping coefficient rises rapidly, which agrees with the working characteristics of the shear walls. At this stage, the equivalent viscous damping coefficient of the composite specimens is equal to or slightly larger than that of cast-in-place specimens.

Under the same shear span ratio, with changes in the axial compression ratio, the energy dissipation capacity of each specimen has a small difference. Under the same axial compression ratio, the equivalent damping coefficient of the specimens with a large shear span ratio increases after yielding, and the energy dissipation capacity is better. Compared with the cast-in-place specimens under the same axial compression ratio, the energy dissipation capacity of the composite specimens is the same, which shows that the composite form has no significant influence on the energy dissipation capacity of the walls.

3.4. Strain Analysis. Throughout the test, the concrete and steel strain values of each specimen show similar trends. We take the SW1-3 as an example for the analysis of the concrete strain. At the initial stage of loading, the concrete strain on both sides of the specimen and the precast layer only slightly changes. When the horizontal load is applied to the crack load, the strain begins to fluctuate greatly, and microcracks appear on both sides of the specimen. When loading to the ultimate loading scenario, the concrete strain of the precast layer and cast-in-place layer increases significantly and reaches the maximum value, and the strain gauge fails due to the increase in cracks. During the whole test process, the trends of the concrete strain of the precast layer and cast-in-place layer are the same, which shows that the precast layer and cast-in-place layer have a good combination and work

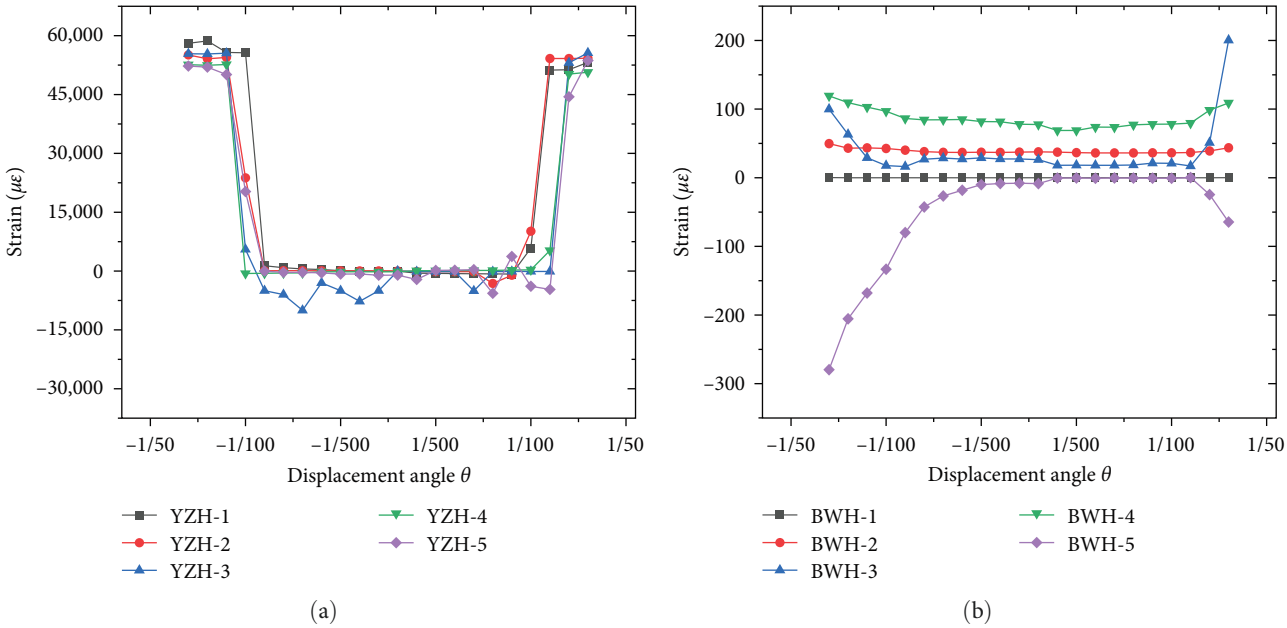

Figure 14: Diagram of the concrete strains of SW1-3: (a) the concrete strains for the precast layer and (b) the concrete strains for the insulation layer.

together (see Figure 14 for the concrete strain of the precast layer and that of the insulation layer). As shown in Figure 14, the concrete strain of the insulation layer is always small, and only a small strain is generated, which shows that the insulation layer did not participate in the structural stress during the test. In the later stage of the horizontal load, BWH-5 exhibited a negative strain value at the lower right corner of the insulation layer. This was due to the wall concrete in that area being crushed, leading to contact between the insulation layer and the ground beam. This situation causes local compression of the area in the lower right corner.

We take the SW2-2 as an example for the analysis of the reinforcement strain. The reinforcement strains are shown in Figure 15. As the load increased, the concrete gradually cracked, and the longitudinal steel strain increased at an accelerating rate. Compared with the longitudinal reinforcement in the wall, the longitudinal reinforcement of the boundary elements has obvious tension and compressive strain, and the strain uniformly increases. The strain of the stirrup increases with increasing displacement angle, which shows that the restraining effect of the stirrup on the concrete increases with an increasing shear wall horizontal displacement. With an axial compression ratio increase, the longitudinal reinforcement peak strain decreases, and the boundary element compressive strain increases. This is because the axial load restrains the development of cracking, the height of the shear–compression zone increases, which counteracts the tensile stress caused by the horizontal load so that the tensile stress of the longitudinal reinforcement in the wall decreases, while the longitudinal reinforcement of the boundary elements exhibits a compressive buckling phenomenon.

4. Numerical Analysis

4.1. Numerical Model. The finite element analysis software ABAQUS is used to conduct a numerical simulation analysis of SW2-1∼3 and W2. The concrete damage plasticity (CDP) model is selected as the constitutive model of concrete, and the relevant elastic–plastic parameters are set in Table 4. The reinforcement constitutive model adopts the reinforcement hysteretic model proposed by Fang et al. [33], as shown in Figure 16, to simulate the bonding and sliding between the concrete and the reinforcement.

The compressive strength, yield strength, and ultimate strength of the concrete in the model are selected according to the measured values. The elastic modulus of the concrete is 3.0×10^4 MPa, the density is 2.4×10^3 kg/m^3, and Poisson's ratio is 0.2; the initial elastic modulus of the steel is 2.06×10^5 MPa, the density is 7.85×10^3 kg/m^3, and Poisson's ratio is 0.3; the tensile strength of the connectors is taken as 50.26 MPa, elastic modulus is taken as 8.3×10^{-3} MPa, density is taken as 1.14×10^3 kg/m^3, and Poisson's ratio is taken as 0.28; the elastic modulus of the graphite extruded board is taken as 9.5 MPa, density is taken as 20×10^3 kg/m^3, and Poisson's ratio is taken as 0.1; the elastic modulus of the vertical rock wool board is taken as 16 MPa, density is taken as 150×10^3 kg/m^3, and Poisson's ratio is taken as 0.13.

The model is modeled in separate parts. The solid element C3D8R is adopted for the concrete, graphite plate, rock wool plate, and connectors, and the truss element T3D2 is adopted for the steel bars.

Combined with the actual design requirements, the main interactions used in this model are embedded, coupling, and

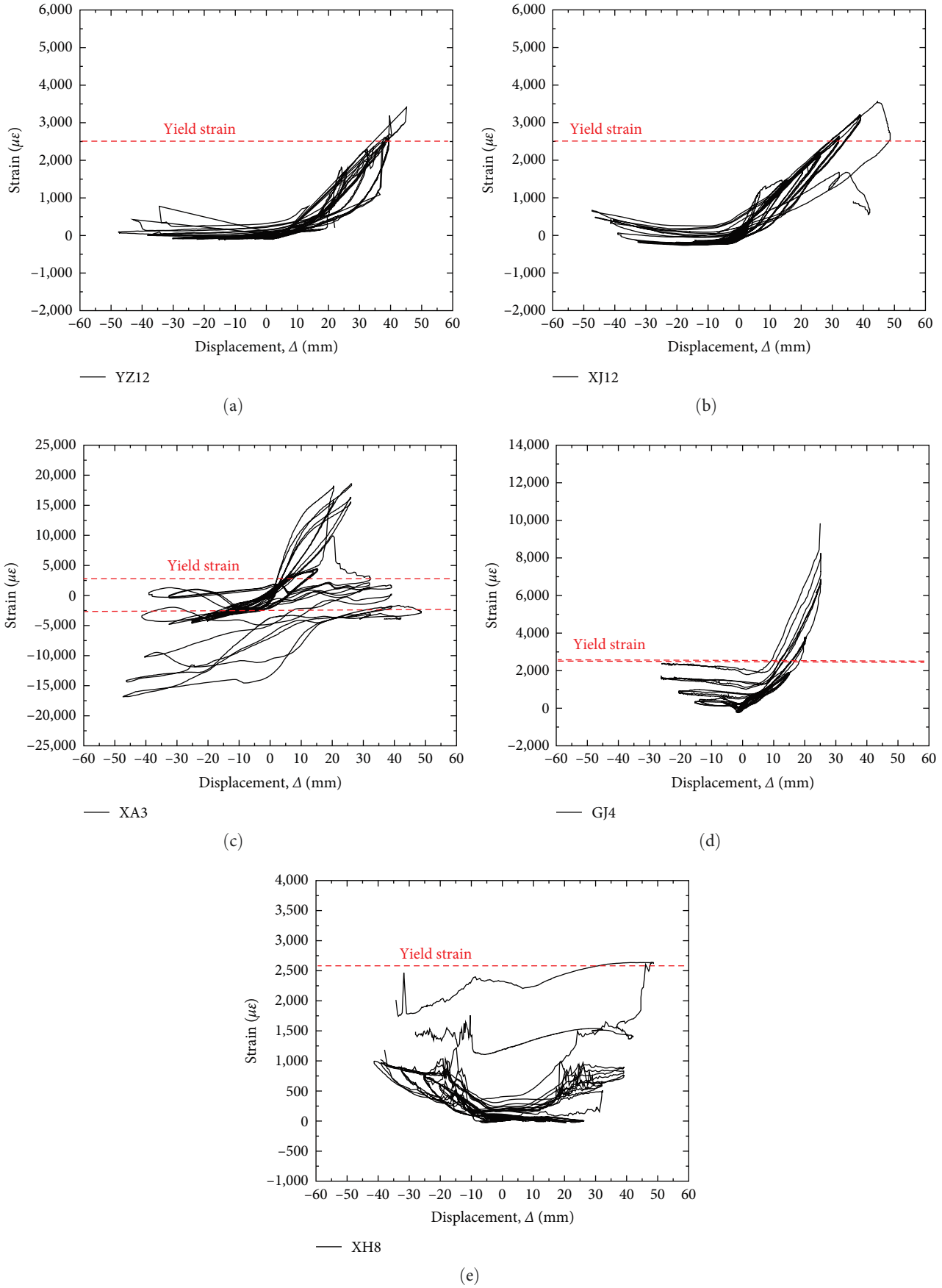

Figure 15: Diagram of the reinforcement strain of SW2-2: (a) the strain of the reinforcement in the precast layer, (b) the strain of the reinforcement in the cast-in-place layer, (c) the strain of the stirrup reinforcement in the boundary element, (d) the strain of the reinforcement in the boundary element, and (e) the strain of the lateral reinforcement.

Table 4: Concrete elastoplastic parameters.

Expansion angle	Offset value, ε	Fb_0/fc_0	K	Viscosity coefficient, η	Poisson's ratio, μ
30	0.1	1.16	0.667	0.005	0.2

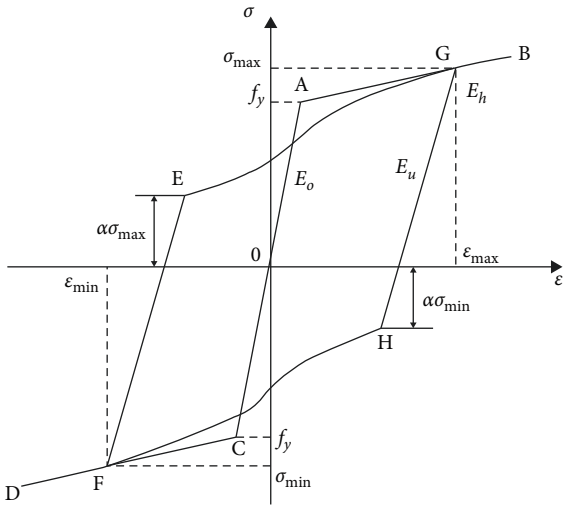

Figure 16: Reinforcement hysteretic model.

contact. The relationship between the reinforcement and concrete in the specimen is defined as embedded. The interface between the precast layer and cast-in-place layer is defined using the cohesive force–friction mixed model, and the interface between the insulation layer, the structural layer, and that which exists between the graphite plate and the rock wool plate are defined using the Coulomb friction model.

This model consists of two analysis steps. In the first step, vertical axis pressure is applied. In the second step, loading displacement is applied, and the loading system is consistent with the test. Two reference points, RP-1 and RP-2, act on the center of the loading surface and side of the roof beam, respectively. The two reference points are coupled with their corresponding loading surfaces, and the displacement in the x direction and the rotation angles in the y and z directions are constrained at the RP-1 reference point. The displacements in the x and y directions and the rotation angles in the y and z directions are constrained at the RP-2 reference point. An axial load is applied to the RP-1 reference point, and a horizontal displacement is applied to the RP-2 reference point. The bottom surface of the floor beam is fully consolidated. The prefabricated panels, cast-in-place layers, insulation layers, and connectors are cut into regular models using the datum plane. A 50 mm grid unit is used to mesh the concrete, steel bars, and insulation layers. Due to the short length of the connectors, a meshing unit of 5 mm is used.

The nonlinearity of the material in this numerical analysis may lead to difficulties in convergence, resulting in significant discrepancies between simulation and experimental results. To ensure convergence of calculation results, it is crucial that the model accurately reflects the real scenario. Therefore, the issue of model convergence can be addressed by analyzing the material constitutive model, contact and interaction, unit selection, and mesh division. The elastic–plastic parameters of concrete are determined based on the "Design Code for Concrete Structures" [34], while the reinforcement constitutive model is established by referencing previous studies [33] to ensure the actual hysteretic curve exhibits pinching. Contact and interaction are achieved using a built-in zone method between reinforcement and concrete to simulate common forces in real scenarios. Coupling between the reference point and loading surface is utilized to replicate realistic loading conditions. According to the simulation method of finite elements, the connection between the connector and the wall, graphite plate and rock wool, and the new and old concrete are all in surface contact. The contact model selects the cohesion–friction hybrid model and defines the viscous behavior, damage, tangential behavior, and parameters such as normal behavior. C3D8R three-dimensional solid elements are utilized for establishing precast panels, cast-in-place layers, graphite boards, rock wool boards, and connectors. T3D2 truss units are employed for reinforcement, stirrups, and inserts in the precast panels and cast-in-place layers. The concrete, reinforcement, and insulation layers are meshed with 50 mm grid units, while the grid division unit for the connectors is set at 5 mm. Through the above modeling method, the numerical calculation results can be better converged, so that the simulation results are consistent with the experimental results.

4.2. Failure Patterns. See Figure 17 for the concrete damage nephogram, steel stress nephogram, and failure modes of SW2-1∼3 and W2. Through performing comparative analysis, the simulated results of the four specimens are consistent with the tests, the tension and compression damage of the concrete appear in the lower part of the wall, and the damage nephogram shows basically an X-shaped cross, which is consistent with the test results. As the load is gradually applied, the longitudinal reinforcement on the outer side of the boundary elements yields, the cracks on both sides extend to the middle of the wall, and the longitudinal reinforcement in the wall yields successively, which is consistent with the concrete compression cracking and peeling and the vertical steel yielding at the bottom of the specimen in the experiment. The nephogram shows that there is no damage to the insulation layer of each component, and there is no obvious displacement or slippage between the cast-in-place layer and the insulation layer. In the test results, the bottom part of the insulation layer is separated from the wall under a high axial compression ratio because the concrete at the bottom edge of the wall collapses seriously under the high axial compression ratio, resulting in the bottom of the insulation layer collapsing. As the axial compression ratio increases, the concrete compression damage range gradually expands, the height of the compression damage in the middle area of the wall

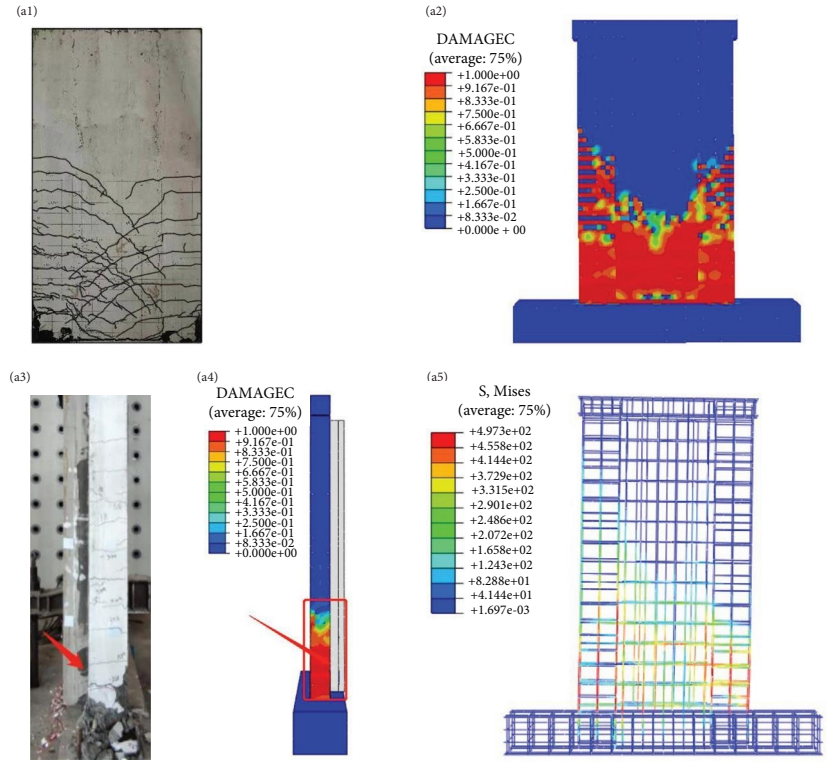

(a)

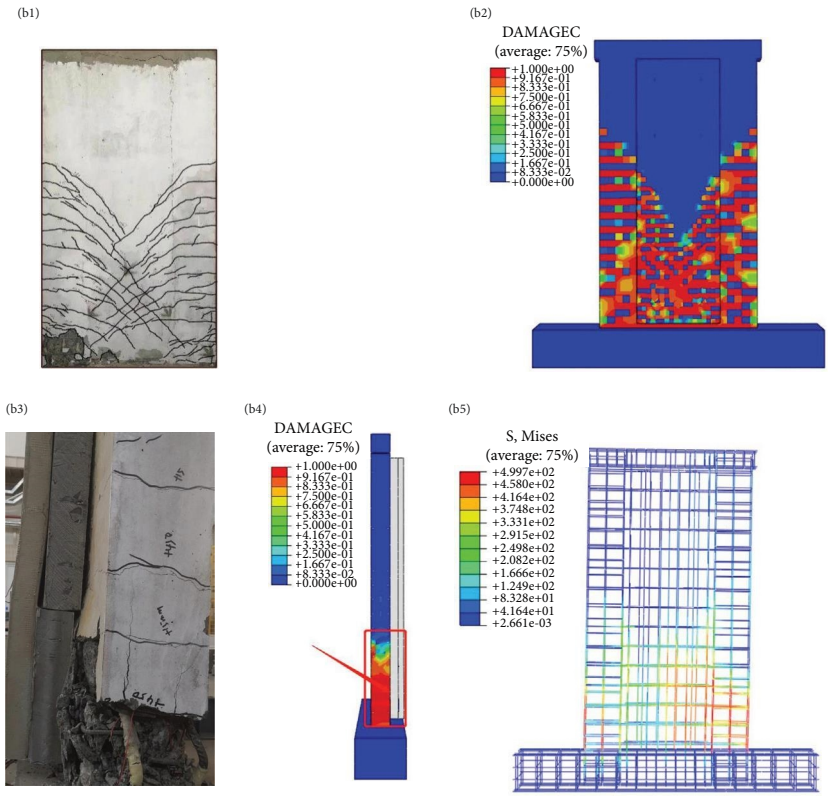

(b)

Figure 17: Continued.

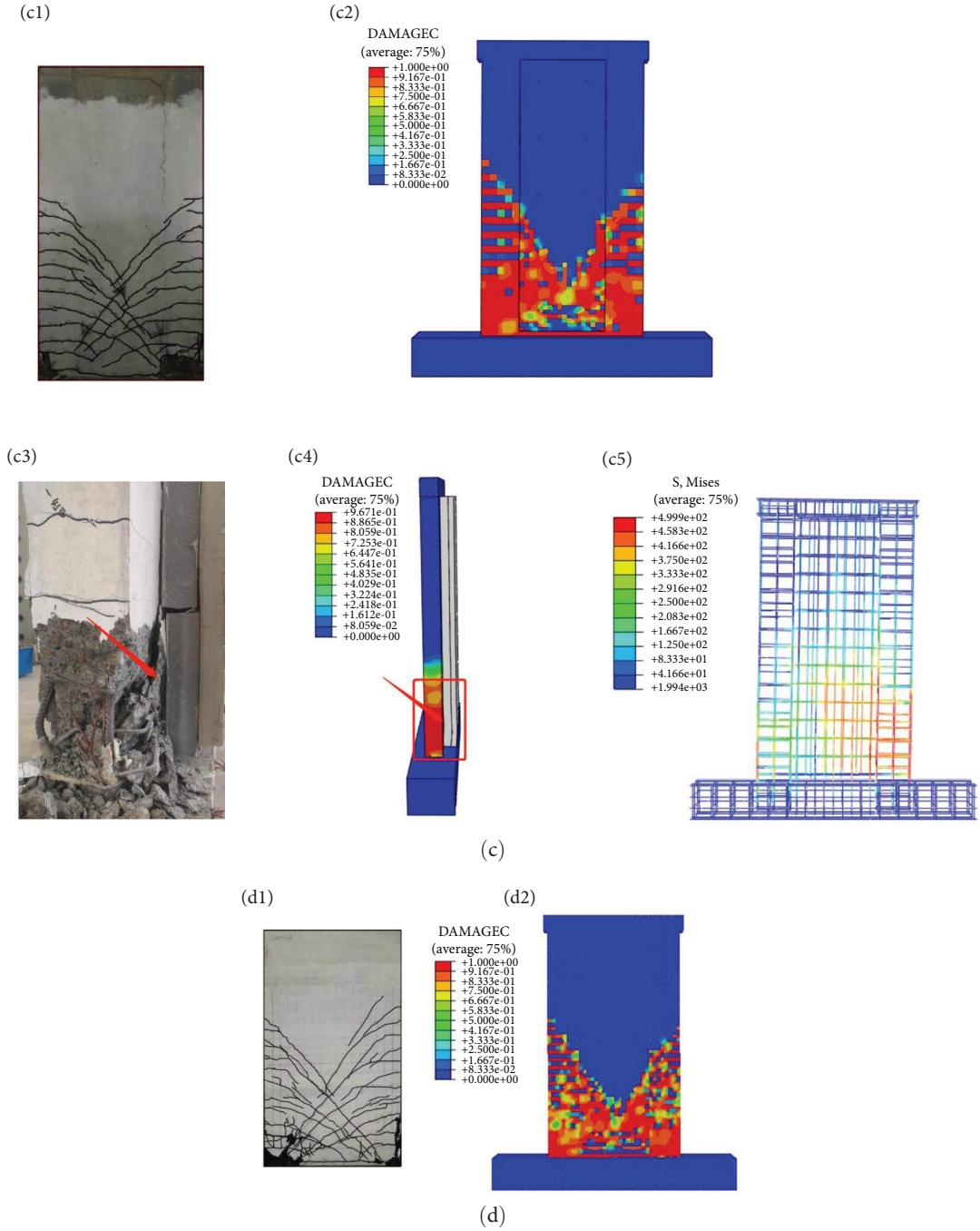

Figure 17: Comparison diagram of the reinforcement stress and the concrete damage between the simulation and the test results. (a) SW2-1. (b) SW2-2. (c) SW2-3. (d) W2. (a1–d1) Crack trends of test. (a2–d2) Concrete tension damage nephogram of simulation. (a3–c3) Concrete damage of test. (a4–c4) Concrete compression damage nephogram of simulation. (a5–c5) Reinforcement stress of simulation.

increases, the tension damage area decreases and the height decreases, and the stress value of the longitudinal reinforcement in the boundary elements and the insert reinforcement to the pedestal increases significantly, and more of the reinforcement reaches the yield value when the specimen is destroyed.

4.3. Hysteresis Curve and Skeleton Curve. Figure 18 shows the hysteresis curve comparison of the simulation models and the experimental results. It is easy to see that the hysteresis curve trends obtained by the simulation and test are consistent, and the hysteresis loops maintain symmetry in both the positive and negative directions. The area of the hysteresis loop is slightly larger in the simulation results because the finite element calculation results are more ideal, while there are some initial defects and errors in the test, leading to a faster stiffness degradation rate. The simulation obtained ultimate load and displacement are not much different from the test, which verifies the accuracy of the model.

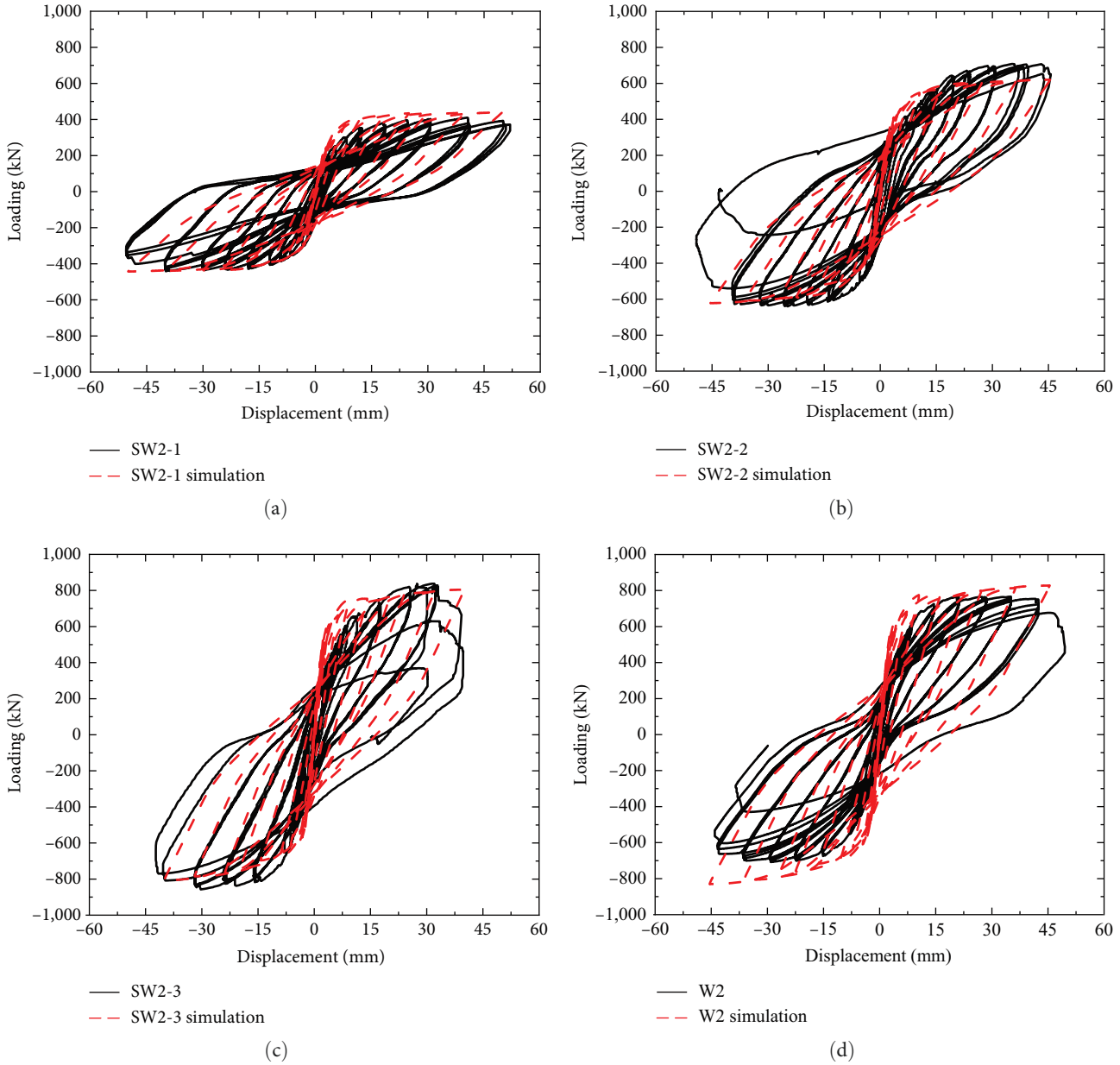

Figure 18: Comparison diagram of the hysteresis curves between the simulation and the test results: (a) SW2-1, (b) SW2-2, (c) SW2-3, and (d) W2.

Figure 19 shows the comparison of the skeleton curve of the simulation models and the test results. It can be seen from Figure 19 that the trend of the simulated skeleton curves of each specimen is the same as the test results, and they all go through elastic and plastic stages. The maximum error between each characteristic point of the simulated skeleton curves and the test values is 10.8%, which is within the allowable error range. The slope of the simulated skeleton curve is larger at the initial loading stage, which indicates that the initial stiffness of specimens is greater at this stage. This is because the simulated boundary conditions are more idealized, and the stress–strain relationship curve specified in the corresponding code is adopted in the simulation, which is different from the actual stress–strain relationship curve of the test. Comparing the test curves with the simulation curves, under the same axial compression ratio, the peak value of the precast specimens is slightly lower than that of the cast-in-place specimens, the trend of the skeleton curves is similar, and the energy dissipation capacity and later occurring stiffness are similar, which shows that the seismic performance of the precast specimens is similar to that of the cast-in-place specimens.

5. Conclusions

In this paper, the failure mode, the hysteresis characteristics, the stiffness degradation, the displacement ductility, and the energy dissipation capacity of six NISCSW specimens and

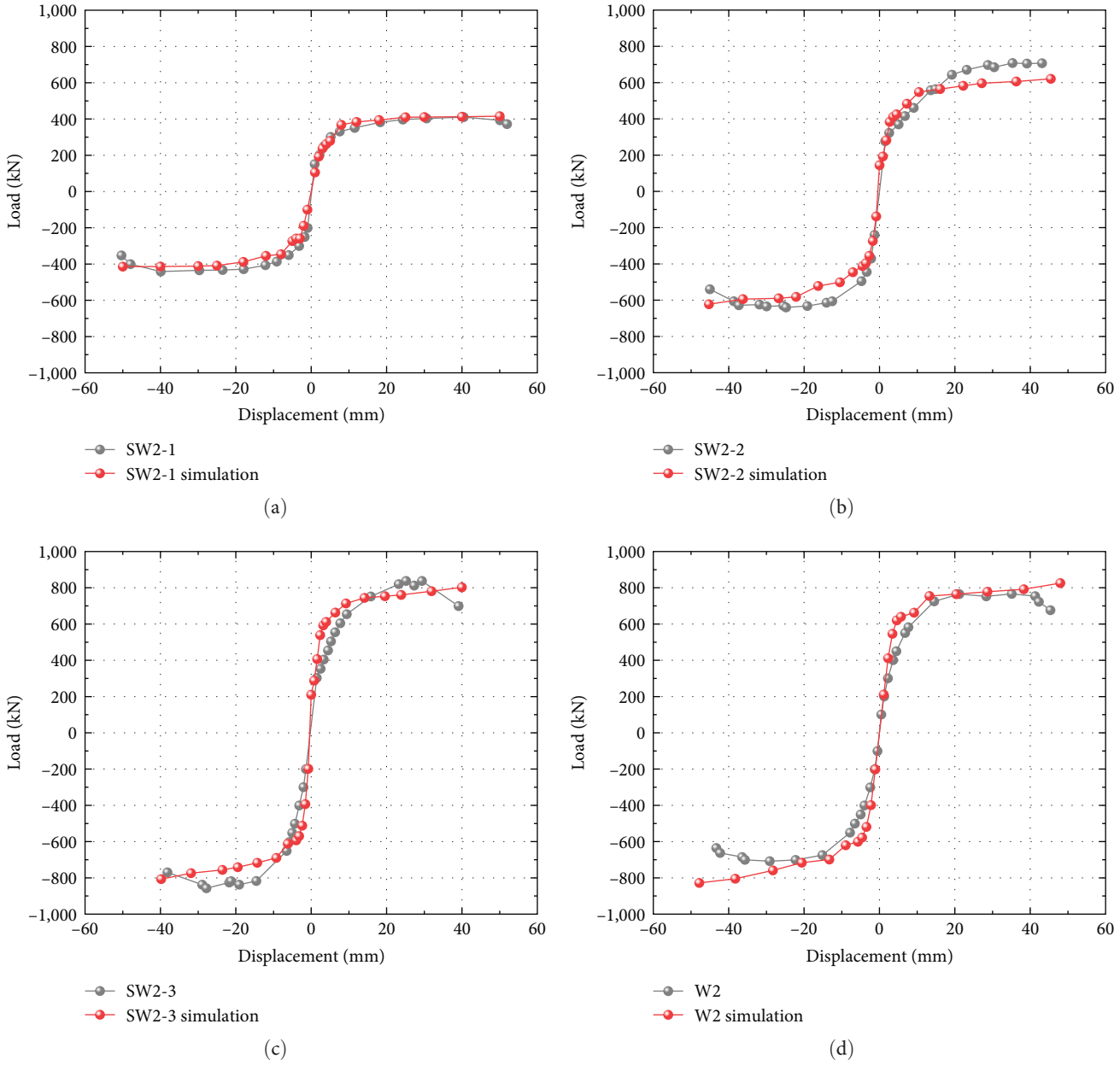

Figure 19: Comparison diagram of the skeleton curves between the simulation and the test results: (a) SW2-1, (b) SW2-2, (c) SW2-3, and (d) W2.

two CCSW specimens are discussed and compared through performing quasistatic tests, and the numerical simulation of the specimens with a shear span ratio of 1.9 is carried out. The conclusions are as follows: (1) The failure mode of the NISCSW specimens is the same as that of the CCSW specimens. With an increase in the shear span ratio, the failure mode of the specimen gradually transitions from a flexural-shear failure to a bending failure, and the distribution height and the intersection position of the cracks in the wall decrease.

(1) In the complete testing process, there is no obvious sliding deformation between the precast layer and the cast-in-place layer, which shows that the precast layer and the cast-in-place layer can work together. There is no obvious crack propagation or peeling on the surface of the insulation layer, which shows that the connector works well, and the insulation layer and the structural wall can form a whole unit and work together, but the insulation layer does not participate in the stress. In the failure stage of the specimen, the insulation layer and the structural layer collapse at the bottom under the high axial compression ratio condition, which is caused by the concrete crushing at the root of the wall.

(2) The hysteresis curve and skeleton curve of the NISCSW specimens are consistent with those of the CCSW specimens, with a little higher initial stiffness and faster stiffness degradation and a similar later stiffness, overall seismic performance, displacement

ductility, and energy dissipation capacity to the CCSW specimens.

(3) Under the condition of the same shear span ratio, the ultimate bearing capacity of the specimen that has a high axial compression ratio is higher and the ductility is slightly worse, but the ultimate displacement angle still meets the limit value of the displacement angle under the conditions of rare earthquakes specified in the Chinese Code of Seismic Design of Buildings (GB50011-2010) [28]. The stiffness degradation trend of each specimen is the same, and the energy dissipation capacity has little difference

(4) Under the same axial compression ratio condition, the ultimate bearing capacity of the specimens with a large shear span ratio decreases, the initial stiffness is lower, and the stiffness rapidly degenerates, but the displacement ductility and the energy dissipation capacity after yield are better.

(5) Through the finite element numerical simulation analysis of the specimens, the simulated failure mode of the specimen is consistent with the test results, and the trend of the simulated hysteresis curve and the skeleton curve is consistent with the test curves, which shows that the finite element model is correct and reliable, and the results can be mutually verified with the test results.

This study provides an in-depth look at the seismic performance of NISCSW under high axial compression ratios and large shear span ratios. There are relatively few studies in this area. Therefore, this study provides more empirical data for the field, facilitating a better understanding of the performance under such conditions. Moreover, the results of this study hold a significant guiding value for engineering practice. In practical engineering, high axial compression ratios and large shear span ratios are common working conditions, and this study will help engineers design and apply NISCSW more effectively under these conditions.

Despite some important preliminary results achieved in this study, there is still much work to be done. First, future research should consider shear walls with openings. The presence of openings may affect the seismic performance of the wall, which is an important research issue. Second, it is recommended to further study the seismic performance of L-shaped or T-shaped combined wall joints. These complex joints are common in practical engineering, but current research on them is insufficient. Through these studies, we can better understand the seismic performance of NISCSW, to provide more valuable guidance for engineering practice.

Data Availability

The experimental and finite element data used to support the findings of this study are available from the corresponding author upon request.

Conflicts of Interest

The authors declare that there are no conflicts of interest regarding the publication of this paper.

References

[1] B. A. Frankl, G. W. Lucier, T. K. Hassan, and S. H. Rizkalla, "Behavior of precast, prestressed concrete sandwich wall panels reinforced with CFRP shear grid," *PCI Journal*, vol. 56, no. 22, pp. 42–54, 2011.

[2] D. Tomlinson and A. Fam, "Experiential investigation of precast concrete insulated sandwich panels with glass fiber-reinforced polymer shear connectors," *ACI Structural Journal*, vol. 111, no. 3, pp. 595–605, 2014.

[3] I. Choi, J. H. Kim, and H.-R. Kim, "Composite behavior of insulated concrete sandwich wall panels subjected to wind pressure and suction," *Materials*, vol. 8, no. 3, pp. 1264–1282, 2015.

[4] D. Tomlinson and A. Fam, "Analytical approach to flexural response of partially composite insulated concrete sandwich walls used for cladding," *Engineering Structures*, vol. 122, pp. 251–266, 2016.

[5] A. Benayoune, A. A. A. Samad, D. N. Trikha, A. A. A. Ali, and A. A. Ashrabov, "Structural behaviour of eccentrically loaded precast sandwich panels," *Construction and Building Materials, Construction and Building Materials*, vol. 20, no. 9, pp. 713–724, 2006.

[6] A. Benayoune, A. A. A. Samad, A. A. A. Ali, and D. N. Trikha, "Response of pre-cast reinforced composite sandwich panels to axial loading," *Construction and Building Materials*, vol. 21, no. 3, pp. 677–685, 2007.

[7] D. Tomlinson and A. Fam, "Combined loading behavior of basalt FRP–reinforced precast concrete insulated partially-composite walls," *Journal of Composites for Construction*, vol. 20, no. 3, Article ID 04015060, 2016.

[8] T. Sharaf and A. Fam, "Analysis of large scale cladding sandwich panels composed of GFRP skins and ribs and polyurethane foam core," *Thin-Walled Structures*, vol. 71, pp. 91–101, 2013.

[9] G. Woltman, M. Noel, and A. Fam, "Experimental and numerical investigations of thermal properties of insulated concrete sandwich panels with fiberglass shear connectors," *Energy and Buildings*, vol. 145, pp. 22–31, 2017.

[10] C. L. Hofheins, L. D. Reaveley, and C. P. Pantelides, "Behavior of welded plate connections in precast concrete panels under simulated seismic loads," *PCI Journal*, vol. 47, no. 4, pp. 122–133, 2002.

[11] J. Olsen and M. Maguire, *Shear Testing of Precast Concrete Sandwich Wall Panel Composite Shear Connectors*, CEE Faculty Publications, 2016.

[12] X. Lian, X. Ye, D. Wang, Q. Jiang, and L. Chang, "Experimental analysis of seismic behavior of composite slab shear walls," *Journal of Hefei University of Technology*, vol. 32, no. 8, pp. 1219–1223, 2009.

[13] X. Lian, X. Ye, L. Zhang, D. Wang, Q. Jiang, and L. Chang, "Finite element analysis of superimposed slab shear wall," *Journal of Hefei University of Technology*, vol. 32, no. 7, pp. 1065–1068, 2009.

[14] X. Lian, X. Ye, L. Chang, Q. Jiang, and D. Wang, "Analysis on calculation model for seismic damage index of the superimposed slab shear walls," *Journal of Shanghai Jiao Tong University*, vol. 44, no. 6, pp. 739–744, 2010.

[15] Z. Wang, W. Liu, Y. Ye, R. Sun, and W. Wei, "Experimental study on seismic performance of reinforced concrete composite shear walls with openings," *Journal of Architectural Structure*, vol. 33, no. 7, pp. 156–163, 2012.
[16] Z. Wang, W. Liu, W. Wei, and Y. Ye, "Experimental study on seismic behavior of reinforced concrete composite shear wall with level splice," *Journal of Architectural Structure*, vol. 33, no. 7, pp. 147–155, 2012.
[17] Z. Wang, X. Li, Y. Wang, Q. Xu, and W. Zhai, "Experimental study on seismic behavior of reinforced concrete composite shear wall with confined boundary member," *Journal of Central South University*, vol. 47, no. 8, pp. 2759–2767, 2016.
[18] W. Zhang, L. Yang, S. Yu, Q. Zhang, and J. Cui, "Research on key issues of the double-superimposed shear wall: experimental study on seismic performance of horizontal connections," *Journal of Civil Engineering*, vol. 51, no. 12, pp. 28–41, 2018.
[19] G. Dong, Q. Gu, Y. Tan, S. Tian, and H. Gao, "Experimental analysis on the seismic performance of prefabricated double-face superposed shear walls with different horizontal connection," *Vibration and Shock*, vol. 39, no. 2, pp. 107–114, 2020.
[20] W. Zhang, L. Yang, S. Yu, and Q. Zhang, "An analysis of shear capacity on horizontal connections of double superimposed shear wall," *Journal of Tongji University*, vol. 48, no. 1, pp. 7–15, 2020.
[21] X. Shen, W. Ma, X. Chen, W. Zhang, R. Wang, and J. Wang, "Experimental study on seismic performance of the vertical joint seam of superimposed concrete wall panels," *Journal of Hefei University of Technology*, vol. 33, no. 9, pp. 1366–1371, 2010.
[22] J. Li, Q. Fan, Z. Lu, and Y. Wang, "Experimental study on seismic performance of T-shaped partly precast reinforced concrete shear wall with grouting sleeves," *The Structural Design of Tall and Special Buildings*, vol. 28, no. 13, pp. e1632–e1645, 2019.
[23] J. Li, Y. Wang, Z. Lu, and J. Li, "Experimental study and numerical simulation of a laminated reinforced concrete shear wall with a vertical seam," *Applied Sciences*, vol. 7, no. 6, pp. 629–648, 2017.
[24] Z. Lu, Z. Wang, J. Li, and B. Huang, "Studies on seismic performance of precast concrete columns with grouted splice sleeve," *Applied Sciences*, vol. 7, no. 6, pp. 571–591, 2017.
[25] Q. Gu, R. Huang, Y. Zhang, Q. Deng, and K. Yang, "Experimental study on out-of-plane mechanical behavior of single-sided composite shear walls with horizontal joints," *Building Structure*, vol. 51, no. 21, pp. 73–80, 2021.
[26] W. Ma, J. Duan, S. Lu, X. Shen, Y. Tan, and M. Gao, "Experimental study on seismic performance of new single faced superimposed slab shear wall with insulating layer," *Building Science*, vol. 37, no. 9, pp. 73–79, 2021.
[27] W. Ma, K. Xu, B. Cheng, Y. Zhang, R. Chen, and D. Chen, "Experimental study on the seismic behavior of a new single-faced superposed shear wall with the concealed column," *Structures*, vol. 33, pp. 4446–4460, 2021.
[28] Q. Jiang, J. Shen, X. Chong et al., "Experimental and numerical studies on the seismic performance of superimposed reinforced concrete shear walls with insulation," *Engineering Structures*, vol. 240, Article ID 112372, 2021.
[29] W.-C. Xue, Y. Li, L. Cai, and X. Hu, "In-plane and out-of-plan mechanical behavior of double faced superposed concrete shear walls," *Engineering Mechanics*, vol. 35, no. 5, pp. 47–53,142, 2018.
[30] Z. Zhao, J. Wang, Y. Yu, Z. Wang, M. Xiao, and Y. Cui, "Experimental study on seismic behavior of double-superimposed shear walls with prefabricated boundary elements under low axial force ratio," *Journal of Architectural Structure*, vol. 42, no. 3, pp. 63–71, 2021.
[31] JGJ/T101-2015, "China architecture & building press," Beijing, China. [in Chinese]
[32] GB50011—2010, "China architecture & building press," Beijing, China. [in Chinese]
[33] Z. Fang, Y. Zhen, and X. Li, "Steel hysteretic model of reinforced concrete structures," *Engineering Journal of Wuhan University*, vol. 51, no. 7, pp. 613–619, 2018.
[34] GB50010-2010, "China architecture & building press," Beijing, China, Beijing, China. [in Chinese]